Geochemistry Geophysics Geosystems G3

Article
Volume 13, Number 8
25 August 2012
Q08014, doi:10.1029/2012GC004163
ISSN: 1525-2027

Published by AGU and the Geochemical Society

Effects of variable magma supply on mid-ocean ridge eruptions: Constraints from mapped lava flow fields along the Galápagos Spreading Center

Alice Colman and John M. Sinton
Department of Geology and Geophysics, University of Hawai'i at Mānoa, 1680 East West Road, Honolulu, Hawaii 96822, USA (acolman@hawaii.edu)

Scott M. White and J. Timothy McClinton
Department of Earth and Ocean Sciences, University of South Carolina, 701 Sumter Street, Columbia, South Carolina 29208, USA

Julie A. Bowles
Institute for Rock Magnetism, University of Minnesota, 100 Union Street SE, Minneapolis, Minnesota 55455, USA

Kenneth H. Rubin
Department of Geology and Geophysics, University of Hawai'i at Mānoa, 1680 East West Road, Honolulu, Hawaii 96822, USA

Mark D. Behn
Woods Hole Oceanographic Institution, 360 Woods Hole Road, Woods Hole, Massachusetts 02543, USA

Buffy Cushman
La Pietra Hawaii School for Girls, 2933 Poni Moi Road, Honolulu, Hawaii 96815, USA

Deborah E. Eason
Department of Geology and Geophysics, University of Hawai'i at Mānoa, 1680 East West Road, Honolulu, Hawaii 96822, USA

Tracy K. P. Gregg
Department of Geology, State University of New York at Buffalo, Buffalo, New York 14260, USA

Karl Grönvold
Nordic Volcanological Center, University of Iceland, Askja, 101 Reykjavík, Iceland

Silvana Hidalgo
Instituto Geofísico, Escuela Polytécnica Nacional, Quito, Ecuador

Julia Howell
Department of Earth and Ocean Sciences, University of South Carolina, 701 Sumter Street, Columbia, South Carolina 29208, USA

Owen Neill
Geophysical Institute, University of Alaska Fairbanks, 903 Koyukuk Drive, Fairbanks, Alaska 99775, USA

Chris Russo
Department of Geology and Geophysics, University of Hawai'i at Mānoa, 1680 East West Road, Honolulu, Hawaii 96822, USA

[1] Mapping and sampling of 18 eruptive units in two study areas along the Galápagos Spreading Center (GSC) provide insight into how magma supply affects mid-ocean ridge (MOR) volcanic eruptions. The two study areas have similar spreading rates (53 versus 55 mm/yr), but differ by 30% in the time-averaged rate of magma supply (0.3×10^6 versus 0.4×10^6 m^3/yr/km). Detailed geologic maps of each study area incorporate observations of flow contacts and sediment thickness, in addition to sample petrology, geomagnetic paleointensity, and inferences from high-resolution bathymetry data. At the lower-magma-supply study area, eruptions typically produce irregularly shaped clusters of pillow mounds with total eruptive volumes ranging from 0.09 to 1.3 km^3. At the higher-magma-supply study area, lava morphologies characteristic of higher effusion rates are more common, eruptions typically occur along elongated fissures, and eruptive volumes are an order of magnitude smaller (0.002–0.13 km^3). At this site, glass MgO contents (2.7–8.4 wt. %) and corresponding liquidus temperatures are lower on average, and more variable, than those at the lower-magma-supply study area (6.2–9.1 wt. % MgO). The differences in eruptive volume, lava temperature, morphology, and inferred eruption rates observed between the two areas along the GSC are similar to those that have previously been related to variable spreading rates on the global MOR system. Importantly, the documentation of multiple sequences of eruptions at each study area, representing hundreds to thousands of years, provides constraints on the variability in eruptive style at a given magma supply and spreading rate.

Components: 16,800 words, 13 figures, 2 tables.

Keywords: Galapagos Spreading Center; lava flow; mid-ocean ridges; submarine volcanism.

Index Terms: 3035 Marine Geology and Geophysics: Midocean ridge processes; 8427 Volcanology: Subaqueous volcanism; 8486 Volcanology: Field relationships (1090, 3690).

Received 5 April 2012; **Revised** 11 July 2012; **Accepted** 13 July 2012; **Published** 25 August 2012.

Colman, A., et al. (2012), Effects of variable magma supply on mid-ocean ridge eruptions: Constraints from mapped lava flow fields along the Galápagos Spreading Center, *Geochem. Geophys. Geosyst.*, *13*, Q08014, doi:10.1029/2012GC004163.

1. Introduction

[2] Although mid-ocean ridge (MOR) magmatism is estimated to account for 75% of the recent global magmatic budget [*Crisp*, 1984], volcanic eruptions on submarine MOR's are notoriously difficult to observe directly, and their study necessitates a variety of unconventional approaches. Along the global MOR system, the products of only about two-dozen submarine eruptions have been mapped previously [*Sinton et al.*, 2002; *Soule et al.*, 2007; *Rubin et al.*, 2012; *Caress et al.*, 2012, and references therein]. Among these examples, observed and inferred variations in eruption rate, size, and frequency correlate reasonably well with variations in spreading rate [*Perfit and Chadwick*, 1998; *Sinton et al.*, 2002]. For most ridges, where crustal thickness is relatively constant, spreading rate and magma supply necessarily co-vary over thousand to million year timescales [*Canales et al.*, 2000; *Bonatti et al.*, 2003], although shorter-term fluctuations about the steady value are also known [*Sinton et al.*, 2002; *Stakes et al.*, 2006]. Along the Galápagos Spreading Center (GSC), however, the Galápagos hot spot causes a significant increase in magma supply to the crust at roughly constant spreading rate, relative to non-hot spot influenced ridges. The GSC thus provides a rare opportunity to study the effects of magma supply on MOR eruptions, independent of variations in spreading rate.

[3] Many models proposed for MOR evolution based on field observations and geologic mapping

[e.g., *Ballard and van Andel*, 1977; *van Andel and Ballard*, 1979; *Perfit and Chadwick*, 1998], bathymetry [e.g., *Kappel and Ryan*, 1986], and numerical modeling [e.g., *Ito and Behn*, 2008] suggest that activity along individual ridges might alternate between predominantly tectonic and magmatic phases. As such, a given ridge segment is likely to be constructed of eruptive units emplaced at a variety of crustal stress states, and fed by magmatic systems that might vary in reservoir volume, crystallinity, temperature, depth, and connectivity. The products of individual volcanic eruptions provide snapshots of magmatic systems and eruptive processes at specific times in the evolution of a spreading center.

[4] Chemically heterogeneous lava flow fields from individual eruptions along the East Pacific Rise (EPR) [e.g., *Bergmanis et al.*, 2007; *Goss et al.*, 2010] have been interpreted to reflect spatial variations in temperature within magma bodies, which could arise from variations in parental magma composition, the frequency of magmatic recharge and eruption, the extent of differentiation, and/ or the efficacy and scales of magmatic mixing [*Rubin et al.*, 1998, 2001; *Sinton et al.*, 2002; *Bergmanis et al.*, 2007; *Goss et al.*, 2010]. Measurements of eruptive volume have been used to place constraints on magma reservoir size and eruption recurrence intervals [*Perfit and Chadwick*, 1998; *Sinton et al.*, 2002]. Variations in lava morphology [e.g., *Fundis et al.*, 2010], lengths of eruptive fissures [*Gregg et al.*, 1996; *Sinton et al.*, 2002; *Ferguson et al.*, 2010], and the partitioning of magma between intrusive and extrusive emplacement regimes [e.g., *Ferguson et al.*, 2010] have been used to understand the evolution of magmatic transport processes and local stress fields during the course of individual eruptive episodes.

[5] Relatively few MOR eruptions have been studied in detail [*Rubin et al.*, 2012]. Most studies have occurred in response to evidence acquired during the course of seafloor investigations [e.g., *Haymon et al.*, 1993; *Auzende et al.*, 1996, *Caress et al.*, 2012], or detected remotely by oceanographic surveys [e.g., *Embley et al.*, 1991; *Chadwick et al.*, 1995] or seismic monitoring [*Fox et al.*, 1995; *Dziak and Fox*, 1999; *Fox*, 1999]. Lavas sampled from these eruptions are generally young enough that they can be dated with high-precision radiometric techniques, providing constraints on eruptive chronologies and recurrence intervals [*Rubin et al.*, 1994, 1998, 2012; *Bergmanis et al.*, 2007]. The study of very recent eruptions also facilitates detailed mapping and characterization of the associated flow fields because of striking contrasts in flow surfaces and sediment cover between newly erupted and older lavas [*Soule et al.*, 2007; *Fundis et al.*, 2010]. Targeted mapping of individual detected eruptions has proven particularly effective along MOR segments with short eruption recurrence intervals [e.g., *Embley et al.*, 1991; *Chadwick et al.*, 1998; *Embley et al.*, 2000; *Soule et al.*, 2007; *Caress et al.*, 2012].

[6] One disadvantage of the eruption-response approach is that it results in few well-characterized eruptions in a given area [*Rubin et al.*, 2012]. Most flow field mapping in response to detected events has resulted in maps of only the youngest one or two units in the area. The longer-term eruptive histories for these areas therefore remain unknown, precluding comparisons of successive eruptions along a given length of the MOR system. In two cases there have been successive documented volcanic events at approximately 15 year intervals: the 1991–2 and 2005–6 eruptions along the northern EPR near 9°50′N [*Haymon et al.*, 1993; *Tolstoy et al.*, 2006], and the 1998 and 2011 eruptions of Axial Seamount along the Juan de Fuca Ridge (JdFR) [*Embley et al.*, 1999; *Caress et al.*, 2012]. These cases provide glimpses of the slightly longer-term evolution of magmatic systems.

[7] Regional mapping campaigns can contribute greatly to our understanding of MOR eruptive processes by documenting the variations in eruptive activity that occur at a given location, even in the absence of "historic" eruptions [*Sinton et al.*, 2002]. For example, *Bergmanis et al.* [2007] identified the five most recent eruptive units along a portion of the southern EPR near 17°30′S and showed that significant variations in mantle source composition and the extent of mixing in sub-axial magma reservoirs occurred over only a few hundred years. Here, we present the results of geologic mapping investigations in two areas of the GSC (Figure 1) that differ in time-averaged crustal production rates [*Sinton et al.*, 2003] and volcanic morphology [*Behn et al.*, 2004; *White et al.*, 2008]. Our results allow us to constrain the effects of magma supply on the size, frequency, and characteristics of individual eruptive episodes representing hundreds to thousands of years of volcanic activity at each site.

2. Geologic Setting: Galápagos Spreading Center

[8] The western GSC is an east–west-trending, intermediate-spreading-rate ridge that separates the

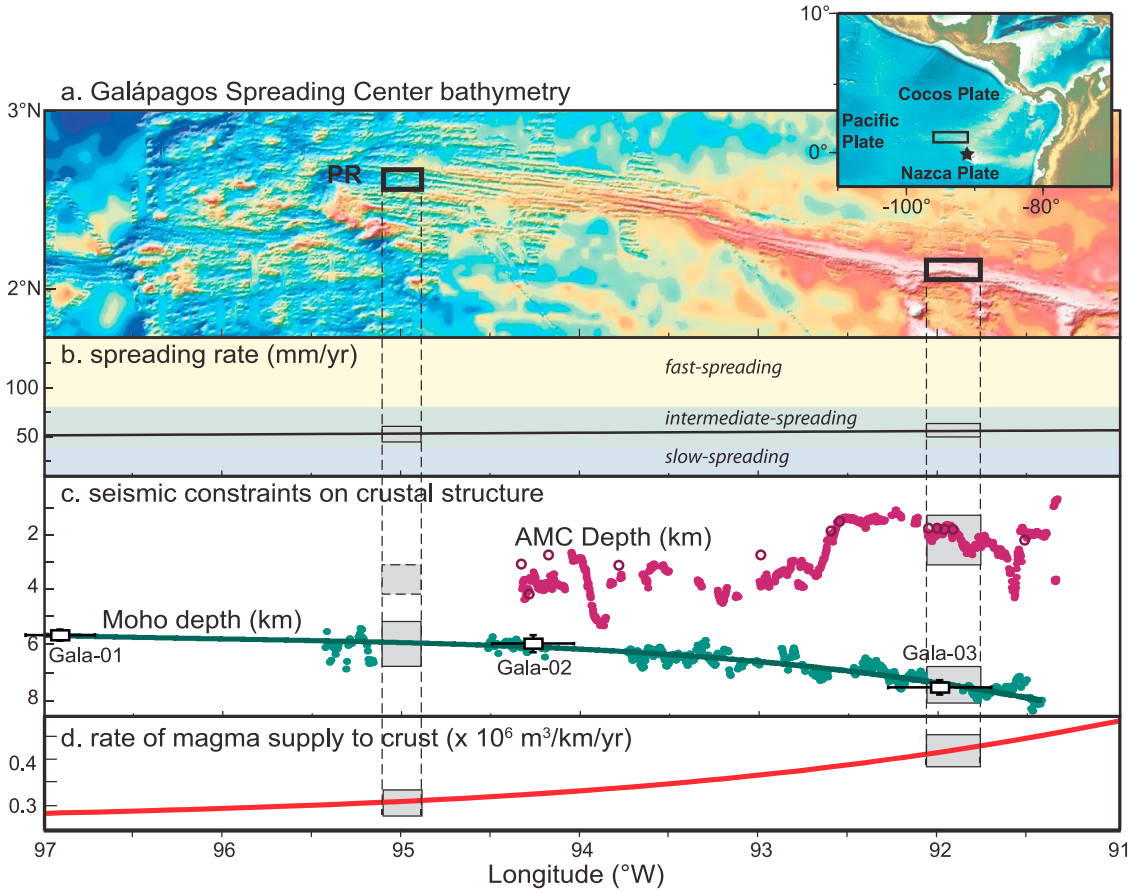

Figure 1. Regional setting and along-axis variations on the western Galápagos Spreading Center (GSC). Inset shows location of study areas relative to Central and South America. Star marks presumed location of Galápagos hot spot. (a) Regional bathymetry based on global compilation of multibeam data merged with satellite-derived bathymetry data [*Ryan et al.*, 2009]. Black boxes outline locations of study areas, shown in Figure 2. PR, propagating rift. (b) Spreading rate [*Argus et al.*, 2011]. (c) Depths of axial magma chamber (AMC) seismic reflector [*Blacic et al.*, 2004] and Moho [*Canales et al.*, 2002]. Solid circles, data from along-axis MCS profiles; open circles, data from cross-axis MCS profiles. Gala-01, Gala-02, Gala-03, data from ocean bottom seismic refraction experiments [*Canales et al.*, 2002]. (d) Crustal production rate calculated as crustal thickness [from *Canales et al.*, 2002] x spreading rate (Morvel [*Argus et al.* [2011]), after *Sinton et al.* [2003].

Cocos and Nazca Plates (Figure 1). The history and morphology of the GSC have been strongly influenced by the presence of the Galápagos hot spot [e.g., *Wilson and Hey*, 1995], which is located ~200 km to the south of the ridge near 91°30′W. Spreading rates along the GSC increase from 48 mm/yr at 100°W to 61 mm/yr at 85°W (Figure 1b) [*Argus et al.*, 2011]. Crustal thickness increases with proximity to the hot spot, reaching ~8 km near 91°30′W (Figure 1c) [*Canales et al.*, 2002]. The seismically imaged axial magma chamber (AMC) deepens away from the hot spot, with no AMC detected west of 94.7°W (Figure 1c) [*Blacic et al.*, 2004]. Other parameters that vary systematically with proximity to the hot spot include axial depth [*Canales et al.*, 2002], axial morphology [*Sinton et al.*, 2003; *White et al.*, 2008], topographic roughness in the axial zone [*Sinton et al.*, 2003], seamount abundance [*Behn et al.*, 2004; *White et al.*, 2008], and the chemical composition [*Cushman et al.*, 2004; *Ingle et al.*, 2010] and crystallinity [*Behn et al.*, 2004] of erupted lavas.

[9] Two study areas with contrasting time-averaged rates of magma supply were selected for detailed geologic mapping of individual lava flow fields in order to investigate the effects of magma supply on MOR volcanic eruptions. The low- and high-magma-supply study areas are located 330 km apart at 95°W and 92°W, respectively (Figures 1 and 2). Over this distance, the average crustal magma supply (calculated as the product of the spreading

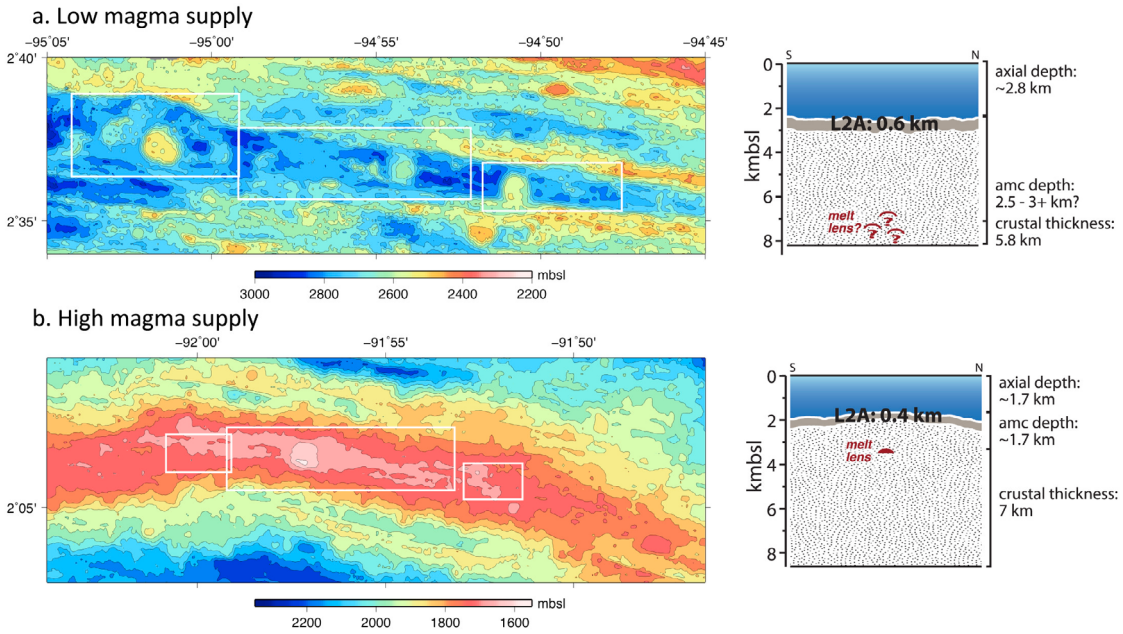

Figure 2. Bathymetric maps and schematic cross-sections of low- and high-magma-supply study areas. Cross-sections summarize structural differences as defined by seismic data [*Blacic et al.*, 2004; *Canales et al.*, 2002]. At low magma supply, the seafloor is deeper, layer 2A is thicker, the crust is thinner, and no melt lens was imaged. White rectangles outline locations of geologic maps presented in Figures 4–9. mbsl, meters below sealevel; kmbsl, kilometers below sealevel. (a) Low-magma-supply study area. (b) High-magma-supply study area.

rate and crustal thickness, after *Sinton et al.* [2003]) increases by roughly one third, from 0.3×10^6 m^3/yr/km to 0.4×10^6 m^3/yr/km (Figure 1d). Short-term spatial and temporal variations in magma supply likely affect both areas, but are unknown in the absence of time series seafloor deformation data or other constraints.

[10] The low-magma-supply study area makes up the western half of the third-order spreading segment M5 of *Sinton et al.* [2003]. A multichannel seismic survey did not detect an axial melt lens in this region; ~35 km to the east, at 94.7°W, a magma lens is 3–4 km deep [*Blacic et al.*, 2004]. A well-defined axial graben at least 2 km wide and 200 m deep is present throughout the 95°W study area (Figure 2a). The axial graben widens to 6 km at the western end of the study area, as it approaches the tip of a westward-propagating rift (Figure 2a) [e.g., *Hey et al.*, 1986; *Sinton et al.*, 2003].

[11] The high-magma-supply study area is roughly centered within the third-order spreading segment E5 of *Sinton et al.* [2003]. A seismically detected melt lens is present at 1.6 km below the seafloor near the center of the segment, deepening to 2 km and 2.4 km at the western and eastern segment ends, respectively [*Blacic et al.*, 2004]. Within this area, the spreading center forms an axial rise that is cut by a shallow axial graben 10–40 m deep (Figure 2b). Differences in axial morphology and crustal structure between the two study areas are summarized in Figure 2.

3. Eruptive Unit Definition and Mapping

[12] Observations of fissure eruptions along divergent plate boundaries in Iceland's Northern Volcanic Zone [*Saemundsson*, 1991; *Wright et al.*, 2012] and Ethiopia's Dabbahu-Manda Harraro Rift [*Ebinger et al.*, 2010; *Wright et al.*, 2012], geologic mapping of submarine lava flow fields along the EPR [*Sinton et al.*, 2002; *Soule et al.*, 2007], and radiometric dating of samples from eruptions along the EPR [*Rubin et al.*, 1994, 2006, 2008; *Bergmanis et al.*, 2007] indicate that at least some lava flow fields are the products of multiple, relatively short-lived (hours to weeks) eruptive events, which collectively comprise longer eruptive episodes lasting months to years. For the purposes of this study, we define a lava flow field as the products of a single eruptive episode, which may comprise the products of multiple eruptive events. Lavas within a mapped flow field should be similar in age, have erupted from a spatially related set of vents, and display petrologic variations that represent co-magmatic

evolution (non-random compositional variation that may reflect variable degrees of fractionation or magmatic mixing). With knowledge of eruption recurrence intervals and sedimentation rates, distinctions can be made among lavas erupted during different eruptive episodes from the past several hundred years, but not necessarily among eruptive events within a single eruptive episode.

[13] In the field, the relative ages of submarine lavas can be assessed using observations of superposition and crosscutting relationships, flow surface preservation, and sediment cover. Freshly erupted lava flows have lustrous, glassy surfaces, on which sediment begins to accumulate immediately [e.g., *Haymon et al.*, 1993]. Sedimentation patterns vary depending on regional slope (steep flanks of mounds tend to shed sediment, which accumulates at their bases) and flow morphology (for high-relief flow morphologies, sediment accumulates first in low-lying pockets, which eventually fill and coalesce) [*van Andel and Ballard*, 1979]. Additionally, hydrothermal activity can locally enhance sedimentation rates [e.g., *Chadwick et al.*, 1998], and bottom currents can redistribute sediment. Bearing in mind these complications, sediment cover on submarine lava flows should be a reasonable proxy for relative age [*van Andel and Ballard*, 1979]. Sediment accumulates relatively quickly along the GSC (1 mm/20–30 years) [*Kleinrock and Hey*, 1989; *Mix et al.*, 1991; *Mitchell*, 1998], allowing distinctions to be made among multiple eruptive episodes within the last several hundred years. Similarly, side-scan sonar data can be used to identify crosscutting relationships between lava flows and fault scarps, and backscatter intensity can be used to assess sediment cover and aspects of flow surface roughness.

[14] Radiometric and geomagnetic paleointensity dating techniques can be used to determine the relative and absolute ages of lava flow fields. Although these techniques are not available in the field, they have been used successfully to confirm that mapped flow fields comprise lavas that are similar in age, and to constrain eruption recurrence intervals [*Bowles et al.*, 2006; *Bergmanis et al.*, 2007] and the chronology of eruptive events within eruptive episodes [*Rubin et al.*, 1994, 1998, 2006].

[15] Lavas erupted during a single eruptive episode are typically delivered to the seafloor via a set of spatially related eruptive fissures, although they need not be contiguous. In some cases, eruptive fissures are visible [*Gregg et al.*, 1996; *Sinton et al.*, 2002; *Soule et al.*, 2007], but elsewhere they are obscured by low effusion-rate lavas and/ or later eruptions [e.g., *Chadwick and Embley*, 1994; *Embley et al.*, 2000; *Sinton et al.*, 2002]. Individual eruptive episodes may include effusion from multiple distinct fissure segments [e.g., *Chadwick et al.*, 1995; *Soule et al.*, 2007]. In the absence of mappable eruptive fissures, vent location can be inferred from lava flow directions [e.g., *Ballard and van Andel*, 1977] and topographic considerations.

[16] At divergent plate boundaries, lavas erupted during individual eruptive episodes commonly have a limited range in modal mineralogy and phenocryst content, and define coherent trends in chemical variation [*Rubin et al.*, 1998; *Rubin et al.*, 2001; *Sinton et al.*, 2002]. The variations, however, can be more complicated than those associated with simple fractionation, as exemplified by the N1 eruption at 17°30′S on the EPR, where magma mixing-controlled variations in magmatic temperature coincide with a third-order discontinuity in the ridge [*Bergmanis et al.*, 2007]. Similarly, the major and trace element compositions of lavas erupted during the 2005–6 eruption at 9°50′N on the EPR vary along the length of an eruptive fissure system spanning several 3rd and 4th order offsets [*Goss et al.*, 2010]. Although many MOR eruptions in Iceland also show coherent spatial-compositional trends [*Sinton et al.*, 2005], complicated magmatic processes appear to be more common in hot spot-affected regions with anomalously thick crust [e.g., *Maclennan*, 2008; *Grönvold et al.*, 2008; *Eason and Sinton*, 2009].

4. Methods

4.1. Field Investigations: AT15–63 Shipboard Operations

[17] In March–April 2010, the Galápagos Ridge Undersea Volcanic Eruptions Expedition (AT15–63, *R/V Atlantis*) carried out geologic mapping at two study areas along the GSC (Figures 1 and 2; see also www.soest.hawaii.edu/gruvee). Observations of the seafloor were made during thirteen dives at each study area (twenty-six total), using the human-occupied submersible *Alvin* (operated by the Woods Hole Oceanographic Institution, WHOI). *Alvin* dive tracks averaged 3.6 km in length, covering a total of ~46 km at each study area. Individual dives visited targets identified from bathymetric maps and previously collected DSL 120A acoustic backscatter data [*White et al.*, 2008]. Divers used relationships of superposition between lava flows and changes in sediment cover, lava flow direction, and lava morphology to infer boundaries between

eruptive units. In addition, 300 rock samples were collected for petrologic study. The submersible was navigated using gyrocompass measurements of heading and Doppler-derived speeds in conjunction with ultra-short baseline (USBL) navigation fixes. Because this navigation system is dependent on communication with the ship, error is accumulated when the submersible loses contact with the ship, for example in close proximity to fault scarps. After the cruise, dive tracks were adjusted manually, where necessary, so that measured depths and diver observations of prominent features were consistent with bathymetric maps.

[18] Night programs during the cruise included photographic surveys and sampling with the deep-towed camera sled *TowCam* [*Fornari*, 2003], and bathymetric surveys using the autonomous underwater vehicle (AUV) *Sentry* (both operated by WHOI). *TowCam* deployments covered 40 km of seafloor (average 2.5 km per tow), and were used both for reconnaissance over potential dive targets, and to visit lower priority locations, frequently farther off-axis. The camera system was towed 5–8 m above the seafloor at a speed of 0.25–0.5 knots, taking color digital photographs of regions ~3–5 m across at 10 s intervals. The camera was connected to the ship via a fiber-optic cable, allowing real-time selection of sampling sites and classification of lava morphology and age relationships. A total of 47 glass samples (wax cores) and 3 rock samples were retrieved with *TowCam.*

[19] *Sentry* was used to map the seafloor at high resolution (1–2 m spatial; <0.5 m vertical) [*McClinton et al.*, 2012]. *Sentry* was equipped with a Reson 7125 400 kHz multibeam sonar system, and operated concurrently with *TowCam.* Flying at 60–80 m above the seafloor, *Sentry* mapped 38 km^2 and 47 km^2 of seafloor at the low- and high-magma-supply study areas, respectively. Mapping of the seafloor at this high resolution reveals morphological details including mounds from which larger volcanic edifices are constructed, lava channels, collapse pits, inflated regions, and even individual hydrothermal chimneys. High-resolution bathymetry data were used to plan *Alvin* and *TowCam* deployments, and to extrapolate observed contacts to regions of the seafloor that were not visited by *Alvin* or *TowCam.*

4.2. Shore-Based Investigations

4.2.1. Lava Composition

[20] Where rock samples were available, they were characterized in hand sample; thin sections were made of selected samples from each eruptive unit. Major element compositions of volcanic glass from 331 samples (including rock samples from *Alvin* and glass chips from *TowCam*) were determined using the University of Hawai'i JEOL JXA-8500F, five-spectrometer electron microprobe. Average compositions and typical mineralogy of samples from each flow field are presented in Table 1. Analytical procedures and the full data set of glass microprobe analyses are available in the auxiliary material.[1]

4.2.2. Geologic Interpretation

[21] Following each *Alvin* dive and *TowCam* deployment, preliminary geologic maps were prepared showing the locations of apparent flow contacts and other features such as faults, fissures, collapse structures, and flow directions. *TowCam* images and screen shots from *Alvin* dive video were assigned locations and geo-referenced. After the conclusion of the cruise, the preliminary geologic maps were used in conjunction with dive videos and transcripts to draw inferred flow boundaries. DSL 120A side-scan sonar data from a December 2005 survey [*White et al.*, 2008] and the high-resolution bathymetry from *Sentry* were used to extend unit boundaries beyond the visually observed contacts, and to help constrain relative ages. Glass composition and sample descriptions were also used to refine flow field boundaries, and to correlate noncontiguous segments of lava flow fields, where consistent with observations of sediment cover.

5. Eruptive Edifice Morphology

[22] Eruptive unit morphologies at the two study areas can be classified on the basis of vertical relief and plan view basal elongation. We use the four edifice morphologies (smooth flows, hummocky ridges, hummocky mounds, seamounts) described by *Head et al.* [1996] along the Mid-Atlantic Ridge (MAR), but note that the sizes of the features observed within our study areas are somewhat different (see below). Both smooth flows and hummocky ridges are elongated parallel to the spreading axis [*Head et al.*, 1996]. Smooth flows are low-relief lava flow fields that typically occur within topographic lows, and may be composed of pillows or sheet flows (Figure 3a) [*Head et al.*,

[1]Auxiliary materials are available in the HTML. doi:10.1029/2012GC004163.

Table 1. Average Chemical Composition and Sample Descriptions for Lavas From GSC Eruptive Units

	SiO_2	TiO_2	Al_2O_3	FeO*	MnO	MgO	CaO	Na_2O	K_2O	P_2O_5	S	Sum	Temp (°C)	Sample Mineralogy
Low Magma Supply														
Frijoles	50.3	1.42	14.1	11.3	0.20	7.48	12.2	2.25	0.13	0.13	0.13	99.6	1175	15–20% plag-phyric; 2–5% ol-phyric
n = 17 σ	0.4	0.07	0.2	0.2	0.01	0.18	0.2	0.03	0.01	0.01	0.00			
Del Norte	49.8	1.27	14.8	10.4	0.18	8.28	12.6	2.11	0.11	0.11	0.12	99.6	1187	<5–15% plag-phyric, 1–2% ol-phyric
n = 25 σ	0.3	0.03	0.1	0.1	0.01	0.07	0.1	0.02	0.00	0.01	0.00			
Buho	49.9	1.45	14.7	11.0	0.19	8.27	11.9	2.25	0.13	0.13	0.13	100.1	1192	< 2 % ol-phyric
n = 28 σ	0.5	0.03	0.2	0.1	0.01	0.22	0.1	0.06	0.00	0.01	0.00			
Tortuga	50.5	1.23	14.7	10.6	0.19	8.13	12.7	2.25	0.08	0.10	0.12	100.8	1189	15–20% plag-phyric; <2% ol-phyric
n = 6 σ	0.1	0.03	0.1	0.1	0.00	0.08	0.0	0.02	0.00	0.00	0.00			
Dragón	49.6	1.26	14.6	10.6	0.18	8.26	12.3	2.12	0.10	0.10	0.12	99.2	1189	3–5% plag-phyric
n = 15 σ	0.3	0.02	0.1	0.1	0.01	0.07	0.0	0.03	0.00	0.01	0.00			
Pulgár	50.6	1.28	14.2	10.8	0.19	7.95	12.6	2.10	0.08	0.10	0.12	100.1	1183	10–15% plag-phyric; <2% ol-phyric
n = 9 σ	0.3	0.02	0.1	0.1	0.01	0.06	0.0	0.02	0.00	0.01	0.00			
Pinguino	51.0	1.38	14.2	11.3	0.19	7.63	12.2	2.15	0.11	0.12	0.13	100.7	1176	<3% ol- and plag-phyric
n = 4 σ	0.3	0.04	0.1	0.2	0.00	0.11	0.1	0.02	0.00	0.01	0.00			
Altares	51.4	1.51	14.4	11.5	0.20	7.42	12.0	2.41	0.14	0.14	0.13	101.3	1171	5–15% plag; <2% ol
n = 10 σ	0.3	0.10	0.1	0.2	0.01	0.21	0.2	0.09	0.02	0.02	0.00			
High Magma Supply														
Ninos	50.5	2.93	13.1	14.9	0.25	4.36	8.77	3.38	0.64	0.41	0.18	99.4	1105	aphyric
n = 29 σ	0.6	0.04	0.1	0.2	0.01	0.10	0.15	0.06	0.02	0.01	0.00			
Calór	50.4	2.04	14.0	12.2	0.20	6.26	10.9	2.75	0.45	0.24	0.14	99.6	1144	aphyric
n = 30 σ	1.4	0.17	0.3	0.3	0.05	0.08	0.2	0.12	0.04	0.06	0.01			
Empanada	50.3	2.79	13.4	14.4	0.24	4.81	9.32	3.27	0.56	0.36	0.17	99.6	1114	aphyric
n = 11 σ	1.5	0.18	0.4	0.6	0.02	0.42	0.35	0.10	0.05	0.03	0.01			
Dulces	53.0	2.52	13.3	13.8	0.24	3.33	7.54	3.55	0.86	0.54	0.14	98.8	1084	aphyric
n = 4 σ	1.1	0.18	0.2	0.1	0.01	0.49	0.58	0.21	0.08	0.04	0.01			
Gusanos	48.8	1.94	14.9	11.2	0.19	7.00	11.9	2.76	0.34	0.22	0.13	99.5	1156	aphyric
n = 3 σ	0.7	0.04	0.2	0.2	0.01	0.16	0.3	0.01	0.01	0.01	0.00			
Iguana	50.6	2.04	14.1	12.2	0.20	6.10	10.9	2.77	0.50	0.25	0.14	99.7	1144	aphyric
n = 11 σ	0.4	0.02	0.1	0.1	0.01	0.08	0.1	0.02	0.01	0.01	0.00			
Cocodrilo	50.6	2.04	14.1	12.2	0.20	6.10	10.9	2.77	0.50	0.25	0.14	99.7	1139	aphyric
n = 11 σ	0.8	0.04	0.2	0.3	0.01	0.16	0.2	0.05	0.02	0.01	0.00			
Lobo del Mar	50.0	2.29	14.6	12.2	0.20	5.98	10.5	3.01	0.41	0.27	0.15	99.6	1139	<1 % plag-phyric
n = 5 σ	0.8	0.04	0.1	0.2	0.00	0.14	0.1	0.06	0.01	0.01	0.00			
Lagarto	48.1	1.71	16.2	10.2	0.17	7.99	11.9	2.56	0.32	0.20	0.11	99.5	1183	aphyric
n = 7 σ	0.3	0.03	0.1	0.1	0.00	0.10	0.07	0.02	0.01	0.00	0.00			
Cobija	49.3	1.89	14.6	11.3	0.19	6.92	11.8	2.71	0.37	0.21	0.13	99.3	1155	aphyric
n = 11 σ	0.6	0.13	0.4	0.5	0.01	0.19	0.36	0.13	0.03	0.03	0.00			

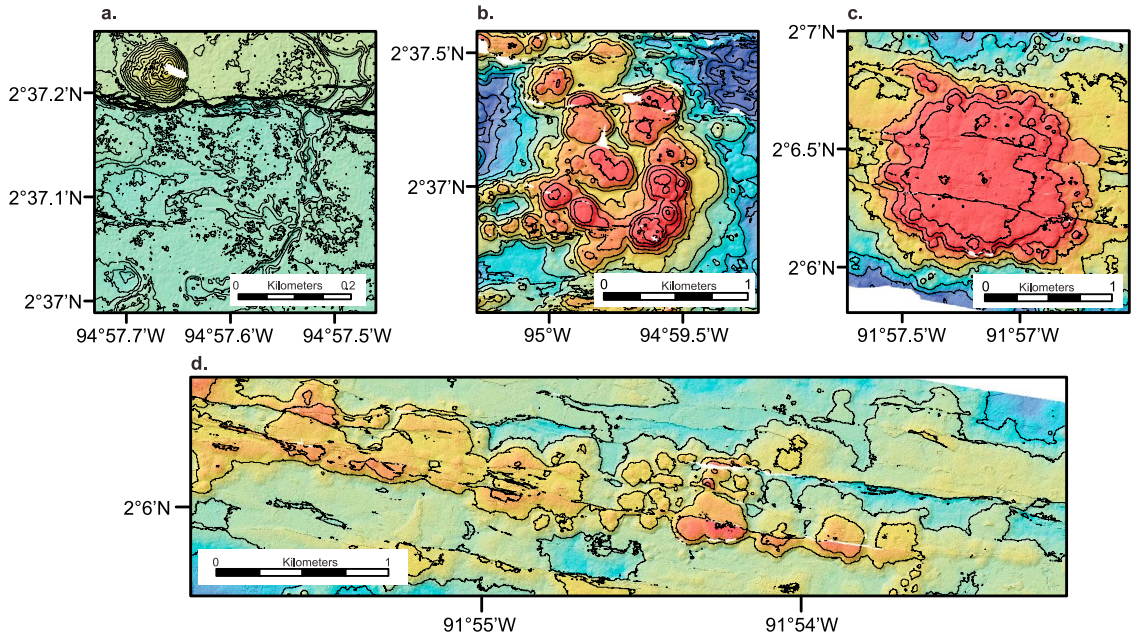

Figure 3. Representative maps of each eruptive morphology classification, after *Head et al.* [1996]. Morphologies are shown as seen in <1 m resolution *Sentry* data [*McClinton et al.*, 2012]. Contour interval: 20 m, except 2 m for smooth flows. (a) Smooth flows. (b) Hummocky mounds. (c) Seamount. (d) Hummocky ridge.

1996]. The inferred eruptive vents feeding these flow fields are aligned along fissures that are up to several kilometers long. Lava is efficiently transported away from the vents via lava channels and inflated lobate lava flows, producing laterally extensive (up to 2.2 km wide) fields. Hummocky ridges have greater relief than smooth flows (maximum 40–50 m tall, except where flow is focused) (Figure 3d). All hummocky ridges observed within our study areas are discontinuous along axis. Several of the hummocky ridges are significantly longer than those observed along the MAR [*Head et al.*, 1996] (2–11 km long within our study areas, versus 1–2.5 km long along the MAR).

[23] Unlike smooth flows and hummocky ridges, hummocky mounds and seamounts are essentially equi-dimensional [*Head et al.*, 1996]. Hummocky mounds are made up of clusters of smaller mounds that may be conical or have small summit plateaus (Figure 3b). The hummocky mounds along the GSC are generally larger than those observed along the MAR (1.5–3 km diameter; 90–200 m tall within our study areas, versus 0.05–0.5 km diameter; <50 m tall along the MAR). Seamounts are more regular in shape, with plateau-like summit regions (Figure 3c); these edifices are associated with the largest-volume eruptions at each study area, and are similar in size to those observed along the MAR (2–2.7 km diameter; 150–300 m tall at our study areas, versus 0.5–3 km diameter; 50–350 m tall along the MAR). Collapse craters are locally present within the summit regions.

6. Eruptive Units

[24] Each study area has been divided into three geographic sub-regions (western, central, and eastern), within which we can constrain relative age relationships among mapped units. Within each sub-region, eruptive units are presented from oldest to youngest. Eruptive units were named based on their appearance in map view or defining characteristics. Three common sediment cover classifications are used [e.g., *Fox et al.*, 1988]: light, moderate, or heavy. Light sediment cover consists of a dusting of sediment on flow surfaces, with slight accumulations in pockets between pillows; sheet flow morphology and details such as striations on pillow lobes are easily discerned. With moderate sediment cover, pockets between pillows contain significant accumulations of sediment (but are not filled); jumbled sheet flow surfaces are partially obscured. Under heavy sediment cover, sediment-filled pockets between pillows are coalescing; lobate and sheet flows are blanketed with sediment such that flow morphology is obscured. The mapped

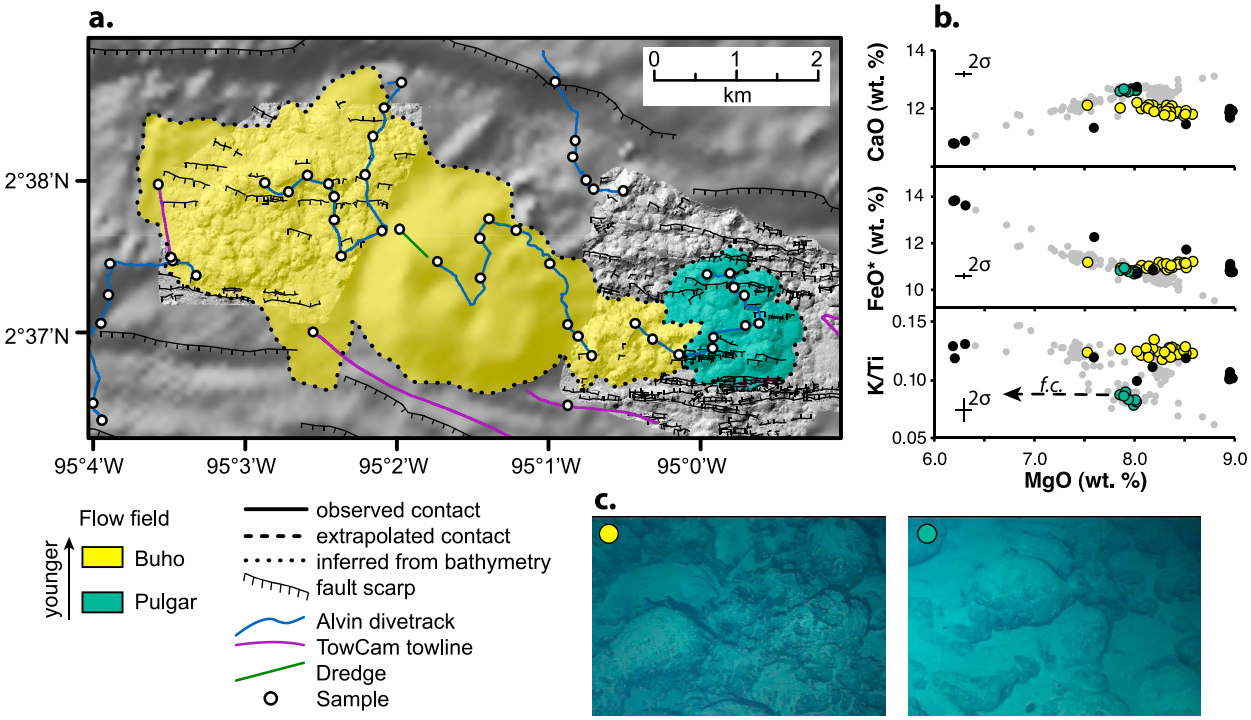

Figure 4. Western region, low-magma-supply study area. (a) Geologic map of region; see legend for symbols. Unit boundaries are symbolized according to how well constrained they are. (b) Compositional fields for eruptive units within the central region. Colors correspond to those used in the geologic map: yellow, Buho; teal, Pulgar; black, other older units; gray, other low-magma-supply samples. Dashed line labeled "f.c." on plot of MgO versus K/Ti shows liquid line of descent predicted by MELTS for fractional crystallization at 500 bars, with oxygen fugacity two log units below the fayalite-magnetite-quartz buffer [*Ghiorso and Sack*, 1995; *Asimow and Ghiorso*, 1998]. (c) Photos of seafloor within each eruptive unit showing typical sediment cover and lava morphology; colors same as in compositional plots.

unit boundaries, major element compositions, and representative outcrop photos are presented in Figures 4–9. A table describing observed hydrothermal features is provided in the auxiliary material.

[25] Samples collected at both study areas are predominantly basalts (less than 52 wt. % SiO_2 [*LeBas and Streckeisen*, 1991]). Fractionation of olivine, plagioclase, and clinopyroxene drives melt compositions to higher FeO* (total iron) and TiO_2 contents until Fe-Ti- oxides become stable at ~4 wt % MgO; basalts with greater than 12 wt. % FeO* and 2 wt. % TiO2 are classified as FeTi basalts, after *Byerly et al.* [1976]. At the low-magma-supply study area, FeTi basalts are rare (2% of samples), whereas at the high-magma-supply study area, they account for half of all samples. Small volumes of basaltic andesite (greater than 52 wt. % SiO_2 [*LeBas and Streckeisen*, 1991]) are present in the eastern sub-region of the high-magma–supply study area (see section 6.2.3, below).

6.1. Low-Magma-Supply Study Area

6.1.1. Western Region (95°04′W–94°59′W) (Figure 4)

[26] Two eruptive units, Buho and Pulgar, were mapped in the northern half of the axial graben shown in Figure 2a. The Pulgar flow field is made up of a cluster of hummocky mounds. The flanks of the mounds are constructed of unornamented, elongate pillows, whereas lobate flows are more common at the summit plateaus of individual hummocks. Samples from Pulgar have 10–15 vol. % plagioclase phenocrysts and less than 2 vol. % olivine phenocrysts, and cluster tightly in composition (7.9–8.0 wt. % MgO). Pulgar has moderate to heavy sediment cover (somewhat heavier at the nearly flat summits of mounds), but heavier sediment and greater fault density on the surrounding seafloor indicate that Pulgar is younger than the regions surrounding it.

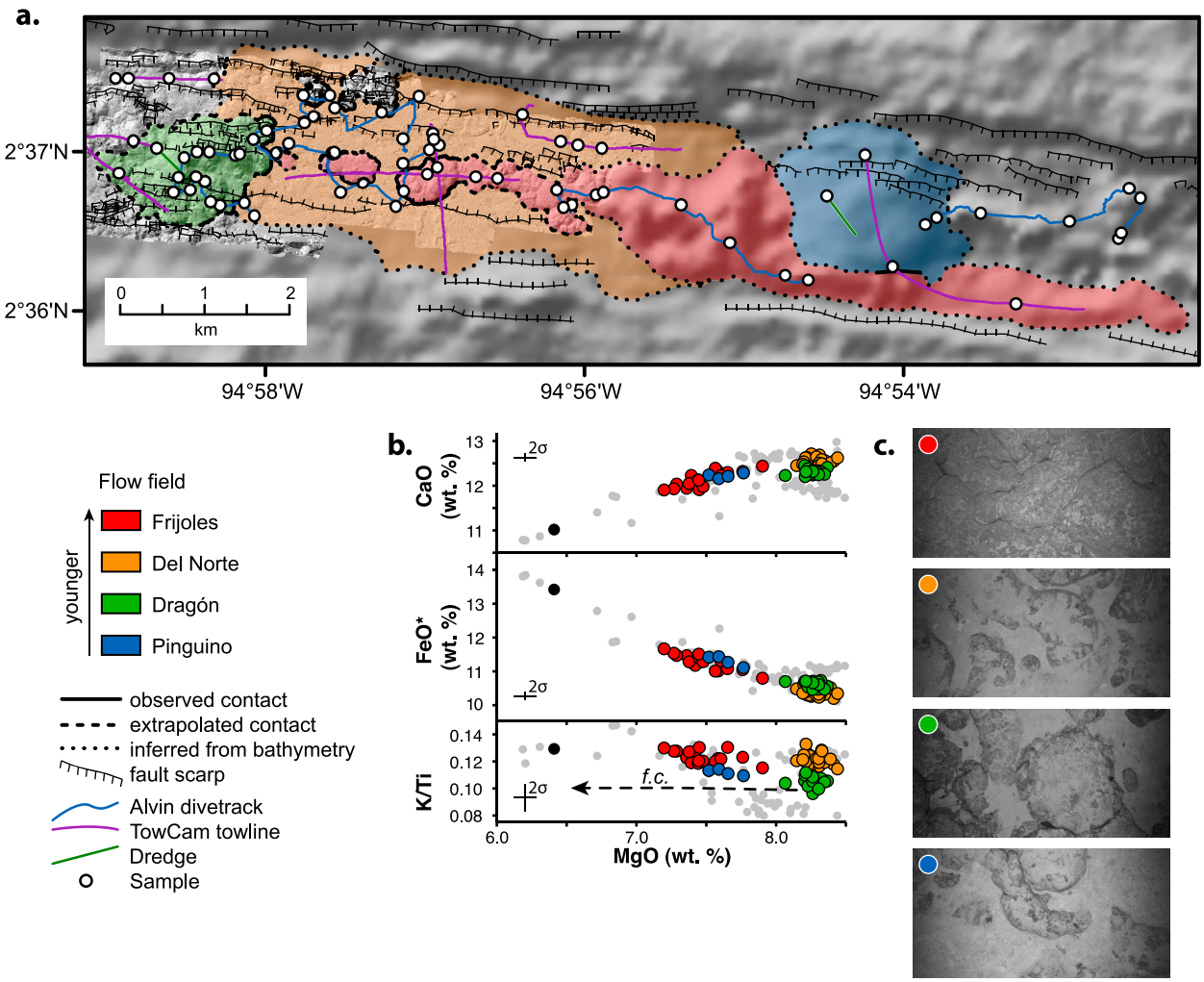

Figure 5. Central region, low-magma-supply study area. (a) Geologic map of region; see legend for symbols. Unit boundaries are symbolized according to how well constrained they are. (b) Compositional fields for eruptive units within the central region. Colors correspond to those used in the geologic map: red, Frijoles; orange, Del Norte; green, Dragón; blue, Pinguino; black, older mound crosscut by Del Norte eruptive fissures; gray, other low-magma-supply samples. Dashed line labeled "f.c." on plot of MgO versus K/Ti shows liquid line of descent predicted by MELTS for fractional crystallization at 500 bars, with oxygen fugacity two log units below the fayalite-magnetite-quartz buffer [*Ghiorso and Sack*, 1995; *Asimow and Ghiorso*, 1998]. (c) Photos of seafloor within each eruptive unit showing typical sediment cover and lava morphology; colors same as in compositional plots.

[27] The Buho flow field is the largest mapped eruptive unit, and comprises an axial seamount 2.6 km in diameter and smaller clusters of hummocky mounds to the east and west. The plateau-like summit region of Buho's central seamount has undulating topography, broken by two collapse craters each 400 m in diameter and greater than 50 m deep. Lavas throughout the flow field have highly ornamented pillow morphology, with abundant cm-scale buds protruding from 1 to 2 m-diameter pillow lobes. Samples are basalts with less than 2 vol. % olivine phenocrysts and greater intraflow compositional variation than Pulgar (7.5–8.6 wt. % MgO). Similar mineralogy and geomagnetic paleointensity of samples collected throughout Buho (J. Bowles, unpublished data) support mapping this large flow field as a single eruptive unit. Buho's light to moderate sediment cover and lower fault density indicate that Buho is younger than Pulgar. At the same MgO content, samples from Pulgar and Buho have different K/Ti ratios (0.09–0.10 and 0.12–0.13, respectively), indicating that they were derived from different parental magmas.

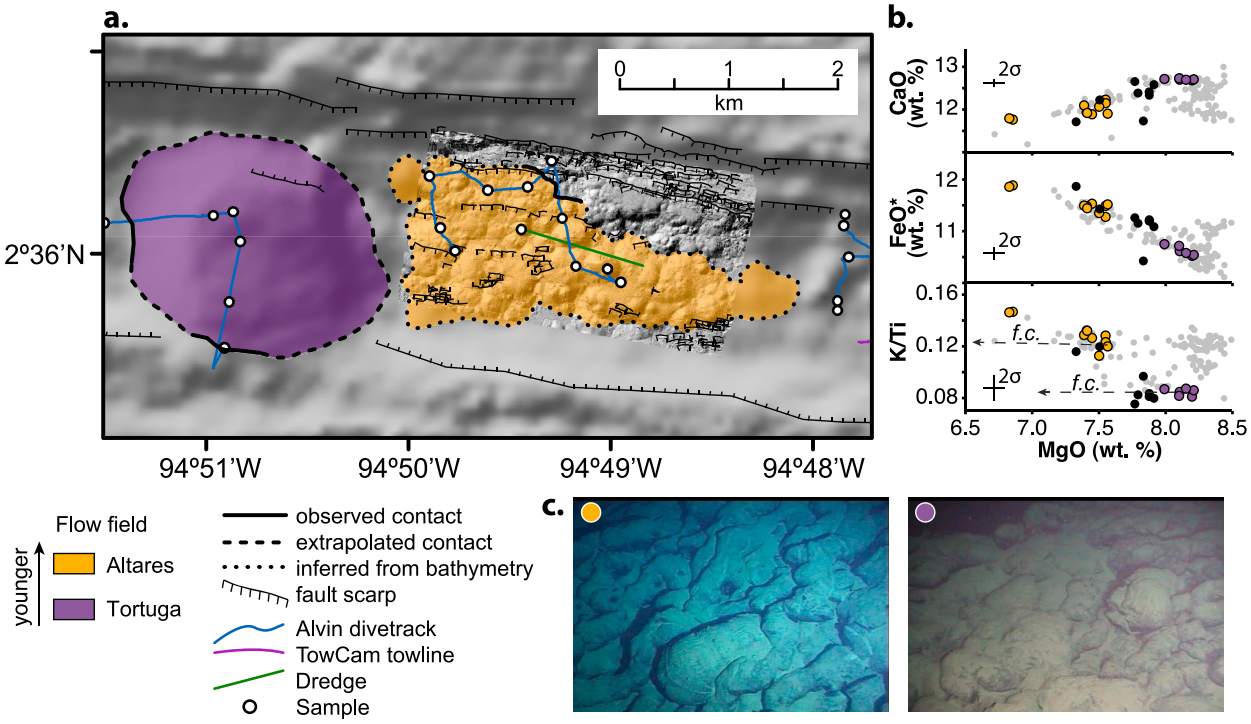

Figure 6. Eastern region, low-magma-supply study area. (a) Geologic map of region; see legend for symbols. Unit boundaries are symbolized according to how well constrained they are. (b) Compositional fields for eruptive units within the central region. Colors correspond to those used in the geologic map: orange, Altares; purple, Tortuga; black, other eastern sub-region lavas younger than Altares; gray, other low-magma-supply samples. Dashed line labeled "f.c." on plot of MgO versus K/Ti shows liquid line of descent predicted by MELTS for fractional crystallization at 500 bars, with oxygen fugacity two log units below the fayalite-magnetite-quartz buffer [*Ghiorso and Sack*, 1995; *Asimow and Ghiorso*, 1998]. (c) Photos of seafloor within each eruptive unit showing typical sediment cover and lava morphology; colors same as in compositional plots.

6.1.2. Central Region (94°59′W–94°52′W) (Figure 5)

[28] A sequence of four mapped lava flow fields in the central region of the low-magma-supply study area exhibits considerable variability in eruptive style. The most prominent eruptive edifice in the central region is Pinguino, an axial seamount 1.7 km in diameter that rises ~200 m above the adjacent graben floor. The northern and southern flanks of Pinguino are cut by east–west-trending faults, and are partially obscured by talus. Side-scan sonar and *TowCam* imagery of the summit region reveal several partially collapsed tumuli; lobate lavas are more abundant at the summit than on the flanks. Samples from Pinguino have 7.5–7.8 wt. % MgO and less than 3 vol. % olivine and plagioclase phenocrysts. The heavy sediment cover observed throughout the summit plateau indicates that Pinguino is the oldest eruptive unit in this sub-region.

[29] The next oldest flow field in the region is Dragón, a relatively small cluster of hummocky mounds that is slightly elongated parallel to the spreading axis, and centered within the axial graben. Dragón's steep flanks are constructed of ornamented pillow lavas. Samples from Dragón define a tight compositional field with 8.2–8.4 wt. % MgO, and have 3–5 vol. % plagioclase phenocrysts. Sediment cover is moderate to heavy even on the steep flanks.

[30] Much of the floor of the axial graben in this sub-region is covered by the broad, gently south-sloping Del Norte flow field, which was erupted from a series of vents near the northern wall of the axial graben and flowed predominantly to the south, where it ponded within the inner axial graben. The areal distribution of Del Norte lava suggests eruption from a fissure at least 3 km long; the eruptive fissures cut through older, compositionally distinct pillow mounds, which are now surrounded by Del Norte lavas. Predominantly north–south-trending lava channels apparently dispersed lava across the axial graben floor. A characteristic stratigraphic sequence of basal sheet flows overlain by lobate flows and small pillow mounds was

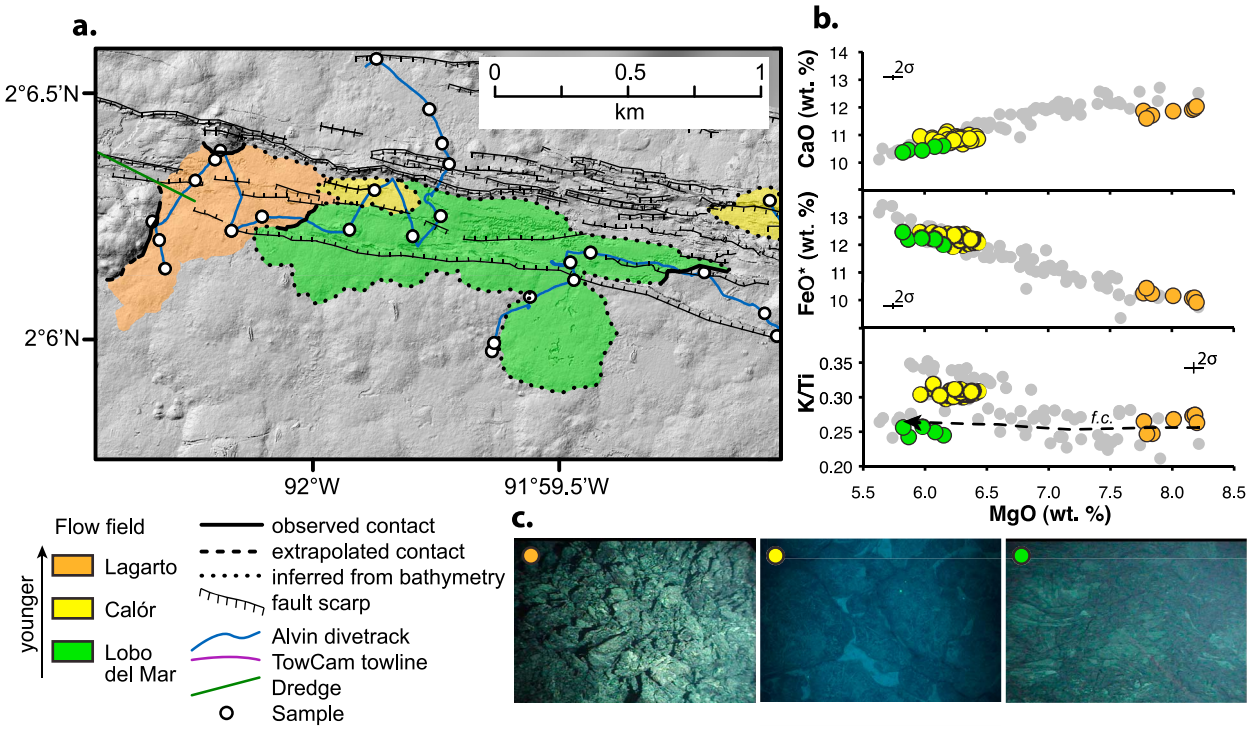

Figure 7. Western region, high-magma-supply study area. (a) Geologic map of region; see legend for symbols. Unit boundaries are symbolized according to how well constrained they are. (b) Compositional fields for eruptive units within the central region. Colors correspond to those used in the geologic map: yellow, Calor; peach, Lagarto; green, Lobo del Mar; gray, other high-magma-supply samples. Dashed line labeled "f.c." on plot of MgO versus K/Ti shows liquid line of descent predicted by MELTS for fractional crystallization at 500 bars, with oxygen fugacity one log unit below the fayalite-magnetite-quartz buffer [*Ghiorso and Sack*, 1995; *Asimow and Ghiorso*, 1998]. (c) Photos of seafloor within each eruptive unit showing typical sediment cover and lava morphology; colors same as in compositional plots.

observed in several locations within this unit, likely indicating decreasing effusion rates as the eruption progressed. Samples from Del Norte are basalts with 5–15 vol. % plagioclase phenocrysts and 1–2 vol. % olivine phenocrysts, and 8.3–8.4 wt. % MgO. In contrast, a sample from the older mound that is cut by Del Norte's eruptive fissures has lower MgO (6.5 wt. %) and is more phenocryst-rich. Del Norte is younger than Dragón, as shown by a high-lava mark (post-drainout feature [*Fornari et al.*, 2004]) of Del Norte lavas ~10 m above the surrounding flow surface on the eastern flank of Dragón, and Del Norte lavas that bury small-offset faults cutting Dragón. Del Norte flows are cut by 10–15 m-high fault scarps at both sides of the graben, indicating that at least some major tectonic event(s) post-dates Del Norte emplacement.

[31] The youngest lavas mapped in the low-magma-supply study area are the Frijoles pillow mounds, which form a discontinuous hummocky ridge centered within the axial graben, ~800 m south of the fissures inferred to have fed the Del Norte eruption. The eastern extent of the Frijoles unit deviates to the south along the flank of the axial graben where Pinguino blocks the middle of the graben. The Frijoles pillow mounds were erupted along a 10.6 km-long eruptive fissure, unlike the more equi-dimensional eruptions that predominate in the study area. *Sentry* bathymetry of the mounds shows that the western mounds have relatively low relief, with broad, nearly horizontal summit plateaus. The eruption appears to have focused near the center of the eruptive fissure, where a large, steep-sided cluster of hummocky pillow mounds reaches heights of nearly 200 m above the surrounding seafloor. Samples range from 7.2 to 7.9 wt. % MgO and contain 15–20 vol. % plagioclase phenocrysts, 2–5 vol. % olivine phenocrysts, and sparse clinopyroxene phenocrysts. The relative age of this youngest unit in the sub-region is confirmed by direct observation of contacts between lightly sedimented Frijoles lavas overlying more heavily sedimented Del Norte lavas in several locations. In addition, *Sentry* bathymetry provides multiple examples of Frijoles mounds that bury Del Norte lava channels and tumuli, and faults that crosscut Del Norte lavas. Yellowish sediment in

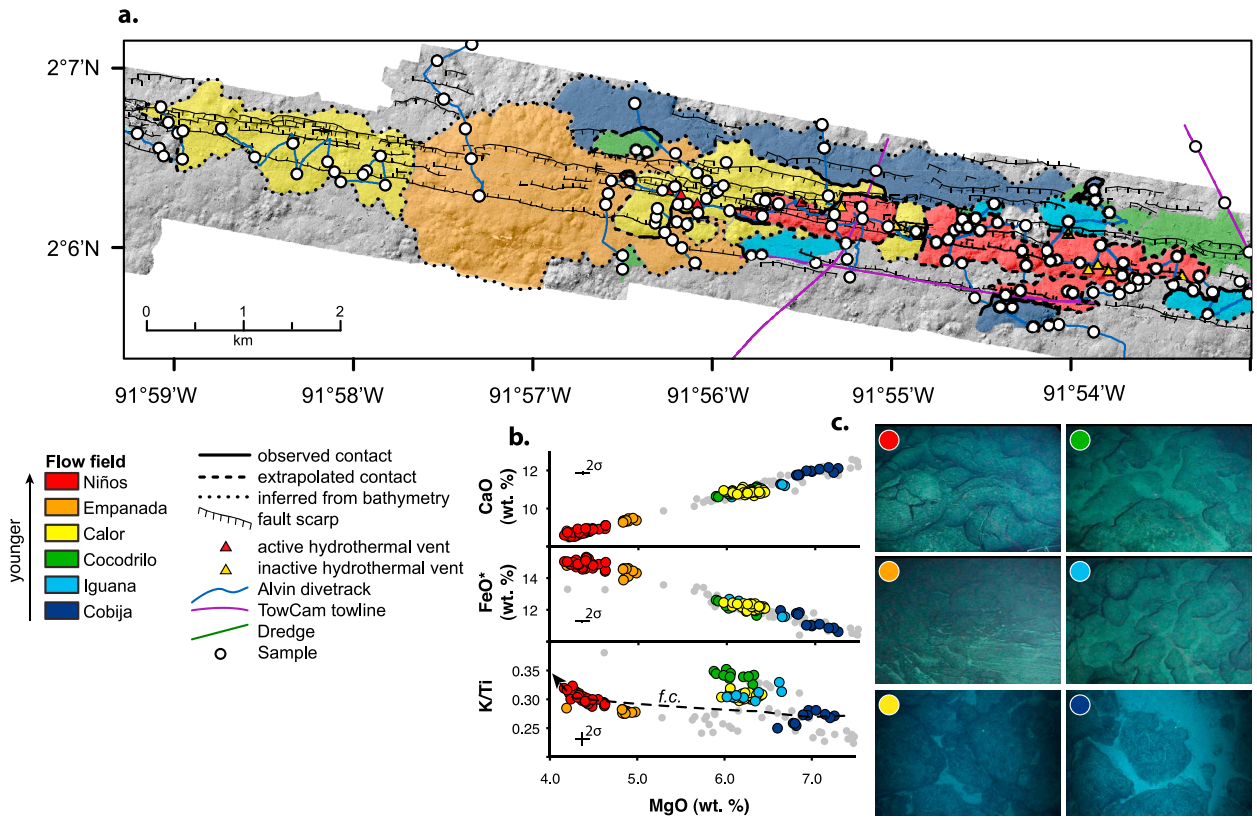

Figure 8. Central region, high-magma-supply study area. (a) Geologic map of region; see legend for symbols. Unit boundaries are symbolized according to how well constrained they are. (b) Compositional fields for eruptive units within the central region. Colors correspond to those used in the geologic map: red, Niños; orange, Empanada; yellow, Calor; green, Cocodrilo; blue, Iguana; purple, Cobija; gray, other high-magma-supply samples. Dashed line labeled "f.c." on plot of MgO versus K/Ti shows liquid line of descent predicted by MELTS for fractional crystallization at 500 bars, with oxygen fugacity one log unit below the fayalite-magnetite-quartz buffer [*Ghiorso and Sack*, 1995; *Asimow and Ghiorso*, 1998]. (c) Photos of seafloor within each eruptive unit showing typical sediment cover and lava morphology; colors same as in compositional plots.

the summit region of some of the mounds suggests the previous occurrence of diffuse flow hydrothermal activity nearby, similar to stains and coatings observed by *Embley et al.* [2000] on the CoAxial segment of the JdFR.

[32] The major and minor element compositions of the four most recent eruptive units in the central subregion of the low-magma-supply study area require at least two parental magmas (Figure 5). Based on these data, it is possible that Frijoles and Del Norte could be related by fractionation of a single parental melt composition. However, the difference in K/Ti between Dragón and Del Norte (0.10–0.11 and 0.12–0.13, respectively) at the same MgO content requires that they were derived from different parental magmas. Variations in the major and minor element compositions within each of these eruptions appear to be consistent with fractional crystallization.

6.1.3. Eastern Region (94°51.5′W–94°48′W) (Figure 6)

[33] A third axial seamount, Tortuga, is located in the eastern region of the low-magma-supply study area. As with the other axial seamounts that were visited, its lower flanks are obscured by an apron of pillow talus. The summit plateau has a mixture of pillow flows and inflated lobate flows similar to features at Pinguino. Deep, east–west trending fissures dissect the summit plateau, exposing pillow and lobate flows. Samples from Tortuga have 15–20 vol. % plagioclase phenocrysts and less than 2 vol. % olivine phenocrysts, with 8.0–8.2 wt. % MgO. Heavy sediment cover suggests that Tortuga is similar in age to Pinguino, Dragón, and Pulgar.

[34] The Altares flow field is the easternmost mapped eruptive unit in the low-magma-supply study area, and consists of a cluster of hummocky

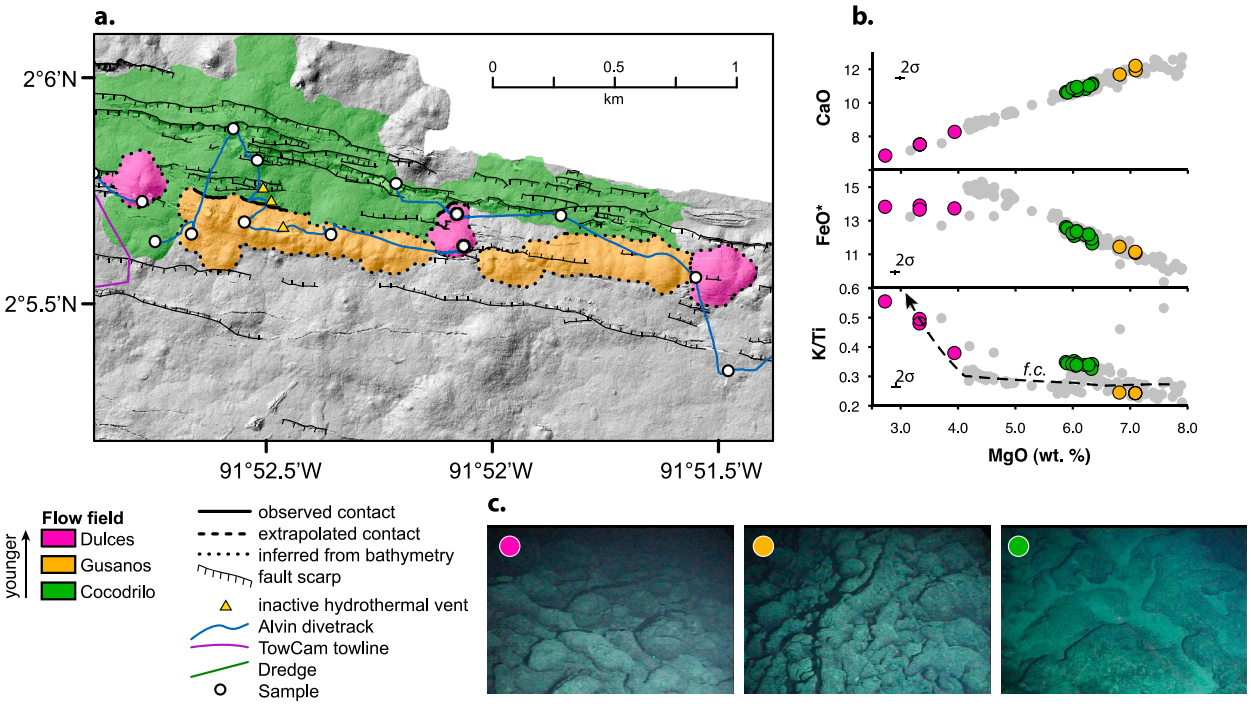

Figure 9. Eastern region, high-magma-supply study area. (a) Geologic map of region; see legend for symbols. Unit boundaries are symbolized according to how well constrained they are. (b) Compositional fields for eruptive units within the central region. Colors correspond to those used in the geologic map: pink, Dulces; orange, Gusanos; green, Cocodrilo; gray, other high-magma-supply samples. Dashed line labeled "f.c." on plot of MgO versus K/Ti shows liquid line of descent predicted by MELTS for fractional crystallization at 500 bars, with oxygen fugacity 1 log unit below the fayalite-magnetite-quartz buffer [*Ghiorso and Sack*, 1995; *Asimow and Ghiorso*, 1998]. (c) Photos of seafloor within each eruptive unit showing typical sediment cover and lava morphology; colors same as in compositional plots.

mounds that is somewhat elongated along a trend oblique to the spreading axis. The flanks of the mounds are mantled with elongate pillow lavas, and lobate flows are more common at the plateau-like summit regions. Samples from Altares have 5–15 vol. % plagioclase and less than 2 vol. % olivine, and contain 7.4–7.6 wt. % MgO. Sediment cover is light to moderate. Near the center of the flow field, a pinnacle built of elongate pillows (apparently erupted at very slow effusion rate) rises ~100 m above the summit plateau. Despite being more evolved compositionally (6.8–6.9 wt. % MgO) than the remainder of the flow field, this pinnacle does not exhibit a significant difference in sediment cover from the rest of Altares. If the pinnacle formed during a later eruptive event, it must have occurred soon after the end of the Altares eruption. K/Ti increases with decreasing MgO in Altares samples, suggesting that compositional variation in this flow field is dominated by magma mixing between at least two variably fractionated batches of magma. The difference in K/Ti between Altares and Tortuga requires different parental magmas for these two units.

6.2. High-Magma-Supply Study Area

6.2.1. Western Region (92°0.5′W–91°59′W) (Figure 7)

[35] The western region of the high-magma-supply study area is intensely faulted, and lacks prominent mounds and ridges, making the identification of flow boundaries difficult. In addition, submersible dives experienced stronger currents throughout the 92°W study area, suggesting that sediment redistribution may be more significant here. Two eruptive units within the western sub-region, Lagarto and Lobo del Mar, are distinguishable mainly on the basis of compositional differences. A third eruptive unit, Calor, is mapped as the westernmost extent of one of the eruptive units in the central region of the high-magma-supply study area (see section 6.2.2, below) based on similarities in composition and sediment cover. The Lobo del Mar flow field erupted from a series of vents aligned along an eruptive fissure near the center of the axial graben. A network of lava channels connects these fissures to a partially collapsed lava lake slightly

south of the axis. Samples from this flow field are FeTi basalts with 5.8 to 6.2 wt. % MgO. Notably, samples from the Lobo del Mar flow field are slightly (≤1%) plagioclase-phyric; samples from every other eruptive unit sampled in the high-magma supply study area are aphyric.

[36] The westernmost mapped flow field in the high-magma-supply study area is the Lagarto flow field, which includes jumbled sheet flows and more laterally extensive regions made up of lobate flows and pillows. In the eastern region of the flow field, there is a north–south-trending channel system within the inner axial graben. Samples from the Lagarto flow field have much higher MgO (7.8 to 8.2 wt. %) than those from Lobo del Mar, although their major and minor element compositions are consistent with derivation from a common parental magma by fractional crystallization. Sediment cover on the two eruptive units is not sufficiently different to assign relative ages.

6.2.2. Central Region (91°59′W–91°53′W) (Figure 8)

[37] Of the six eruptive units that were mapped in the central sub-region of the high-magma-supply study area, Cobija extends the farthest off-axis. Cobija is a smooth lava flow field that consists of a mixture of low-lying pillow, lobate and sheet lavas. Samples from Cobija are aphyric basalts with 6.6–7.3 wt. % MgO. Cobija has heavy sediment cover, and preliminary geomagnetic paleointensity data indicate an eruptive age of ∼400 years [*Bowles et al.*, 2011]. Lavas with similar sediment cover and composition are observed both to the north and south of the axis, and likely belong to the same eruptive episode, with intervening areas buried by more recent eruptive activity.

[38] Moving inward toward the spreading axis in the central region, there are two younger flow fields, Cocodrilo and Iguana. Both flow fields contain a mixture of pillow, lobate, and sheet lavas. Samples from both Cocodrilo and Iguana range from basalts to FeTi basalts (5.9–6.3 and 6.0–6.7 wt. % MgO, respectively), but the two flow fields have different K/Ti ratios (0.33–0.35 and 0.30–0.33), indicating that they either evolved from, or mixed with, different parental magmas. Differences in sediment cover at the boundaries between the two flow fields demonstrate that Cocodrilo is slightly Younger than Iguana. Significant portions of these eruptive units appear to have been buried by younger flows.

[39] Calor is a hummocky ridge that stretches 8.3 km along axis. The off-axis boundaries of the western half of the Calor flow field were not observed, but are presumed to be similar in width to the more extensively mapped eastern half (1 km wide). Calor is less sedimented than Cocodrilo and Iguana, and preliminary geomagnetic paleointensity measurements indicate that they are less than ∼200 years old [*Bowles et al.*, 2011]. Samples from Calor are FeTi basalts that are compositionally similar to those from Iguana (6.0–6.4 wt. % MgO; 0.30–0.32 K/Ti). In April 2010, several high-temperature hydrothermal chimneys were active near Calor's eastern boundary.

[40] The Empanada flow field comprises a broad, 100 m-tall axial seamount and a series of associated sheet flows to the east. The seamount, located near 92°W, is the only relatively large, point-source flow field mapped within the high-magma-supply study area. The flanks of the seamount consist of pillow lavas, whereas lavas at the summit plateau are lobate, with some large, collapsed tumuli that rise 5–10 m above the surrounding flow surfaces. The low-lying sheet flows were erupted from vents just south of the axial graben, apparently during a high-effusion-rate phase before effusion along the eruptive fissure focused to the seamount itself. Samples from both the seamount and the adjacent sheet flows are FeTi basalts (4.2–5.0 wt. % MgO; 0.28–0.29 K/Ti). Although there is not a significant difference in sediment cover between Empanada and Calor and preliminary geomagnetic paleointensity measurements of the two units are indistinguishable [*Bowles et al.*, 2011], Empanada is less faulted than Calor and appears to have buried the middle of the Calor ridge, suggesting that it is younger.

[41] To the east of Empanada and Calor, the Niños flow field forms a discontinuous pillow ridge up to 40 m tall along the spreading axis. The ridge is widest (∼650 m) between 91°54′W–91°55′W, and narrows along axis to both the east and west. The majority of the flow field is composed of pillow lavas. An inflated region and sheet flow extending to the south of the ridge near 91°54′W likely represents the earliest exposed phase of the eruption. Samples from the Niños ridge are FeTi basalts that range from 4.2 to 4.6 wt. % MgO, while those from the sheet flow have 4.5–4.6 wt. % MgO. Niños is only lightly sedimented and is probably the most recent eruptive unit in the central sub-region, although the geomagnetic paleointensity of samples is indistinguishable within error from those of Calor and Empanada [*Bowles et al.*, 2011]. Inward-facing

faults with scarps 10–20 m high cut the Niños field, indicating post-emplacement tectonic activity. Evidence of recent hydrothermal activity abounds within the Niños flow field. Temperatures greater than 300°C were measured in fluids emanating from a cluster of active hydrothermal chimneys (two 9–10 m high, and one smaller chimney) in the western region of the Niños flow field. Extinct chimneys up to 15 m tall, and beds of clam and mussel shells where diffuse venting presumably occurred, occur along fissures and fault scarps throughout the eruptive unit.

6.2.3. Eastern Region (91°53′W–91°51′W) (Figure 9)

[42] Two relatively young eruptive units (Dulces and Gusanos) bury a series of fault scarps that dissect much of the eastern region of the study area. The Gusanos flow field consists of two narrow hummocky ridges (~150 m wide), aligned along the spreading axis. Samples from this unit are aphyric basalts (6.8–7.1 wt. % MgO). Sediment cover is light throughout the unit. Inactive hydrothermal chimneys are present within, and to the north of, the western Gusanos ridge.

[43] At either end of each Gusanos ridge are small (~0.2 km in diameter), equi-dimensional hummocky mounds belonging to the Dulces flow field. The pillows that make up these mounds are large (~1 m in diameter). Samples from Dulces are FeTi basalts and basaltic andesites that are the most fractionated compositions in either study area (2.7–4.0 wt. % MgO) (Table 1), and thin sections contain abundant plagioclase, clinopyroxene, and olivine microphenocrysts. The Dulces mounds appear to postdate the Gusanos ridges, but both units were apparently emplaced relatively recently. A portion of the Cocodrilo flow field extends into the eastern sub-region, but substantially thicker sediment cover and greater fault density (including faults that are buried by Gusanos and Dulces flows) indicate that the Gusanos and Dulces flow fields are younger than Cocodrilo. Lack of flow contacts precludes a more precise definition of the ages of these units relative to the others in the central high-magma-supply study area.

7. Eruption Characteristics

7.1. Lava Composition

[44] Samples from the low-magma-supply study area consistently have higher phenocryst contents than those from the high-magma-supply study area, where phenocrysts were only observed in samples from the Lobo del Mar flow field (Table 1). This observation is consistent with eruption from the seismically imaged melt lens at the high-magma-supply study area, which is expected to contain crystal-poor magma, and from crystal-rich magma reservoirs at lower magma supply, in agreement with the global systematics of MOR's [*Sinton and Detrick*, 1992]. It is notable, however, that the largest flow field in the low-magma-supply area, the Buho flow field, is nearly aphyric. It is presently unclear whether this anomalous eruption was fed from a large, melt-rich magma reservoir or rather from a smaller reservoir that was replenished during the course of the eruption.

[45] At both study areas, mapped eruptive units exhibit only limited compositional heterogeneity with compositional trends that can largely be explained by moderate degrees of fractional crystallization (except within the Altares flow field, where variable K/Ti requires multiple parental magmas). Only two mapped flow fields (Dulces and Buho) have ranges in MgO greater than 1 wt. %. The limited variability of MgO content within individual eruptive units suggests that melt reservoirs are relatively well-mixed, even at low magma supply. For example, the Frijoles flow field extends 10.8 km along axis at the low-magma-supply study area, with only 0.7 wt. % range in MgO and 0.01 in K/Ti, despite previous eruptions in the same region with different MgO and K/Ti contents.

[46] In contrast to the limited compositional variation within eruptive units, there are striking compositional differences between successive eruptions. The common juxtaposition of successive flow fields with compositions that cannot be related by fractional crystallization requires either eruption from separate melt reservoirs within the crust, or magma recharge to the same reservoir(s) occurring at time scales similar to eruption intervals. This observation is consistent with those in *Bergmanis et al.* [2007] for the very-fast spreading southern EPR.

7.2. Lava Temperature

[47] Lava compositions in the high-magma-supply study area have lower average MgO with a wider compositional range than those at low magma supply (average MgO = 6.2 wt. %, range = 5.7 wt. % at high magma supply, compared to 8.0 wt. % and 2.9 wt. % at low magma supply). MgO content decreases with decreasing temperature in basaltic magmas crystallizing olivine + plagioclase ± clinopyroxene. Liquidus temperatures of glass samples from each eruptive

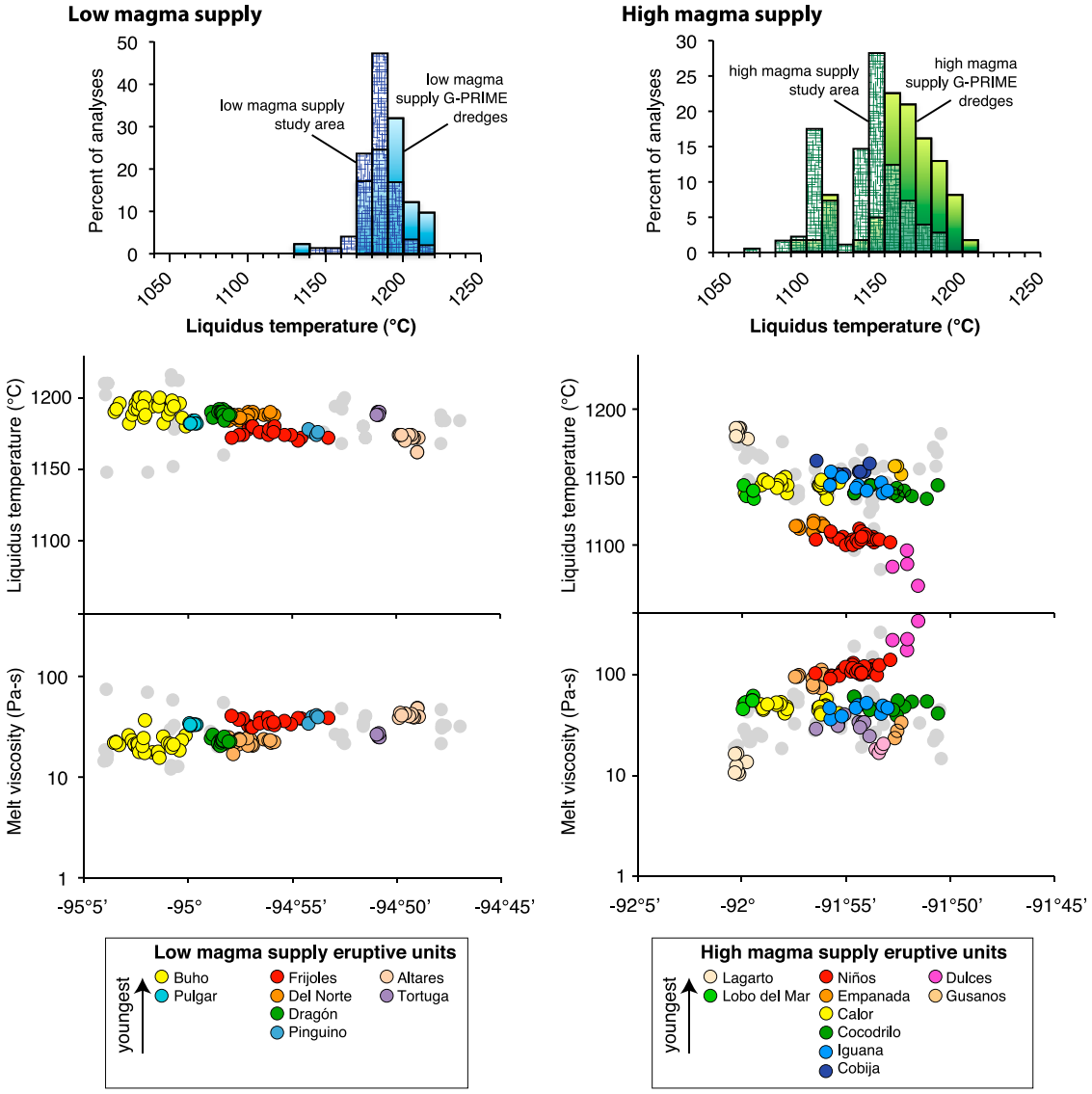

Figure 10. Lava liquidus temperatures calculated using MELTS [*Ghiorso and Sack*, 1995; *Asimow and Ghiorso*, 1998]. (a) Histograms of lava liquidus temperatures at low and high magma supply along the GSC. Patterned bars are samples from low (n = 151) and high (n = 178) magma supply study areas, this study. Solid bars are dredge samples from G-PRIME cruise; low magma supply (n = 40) is taken as west of 94.4°W, where magma supply is <0.3 m^3/km/yr; high magma supply (n = 62) is taken as east of 94.4°W. (b) Liquidus temperature (upper panel) and liquidus melt viscosity (calculated using method of *Giordano et al.* [2008]) of rock samples along axis for low (left) and high (right) magma supply study areas. Colors of dots correspond to eruptive units (see legend at bottom).

unit calculated using MELTS [*Ghiorso and Sack*, 1995; *Asimow and Ghiorso*, 1998] confirm that eruption temperatures of lavas at the high-magma-supply study area are more variable, but cooler on average (1080–1180°C), than those at low magma supply (1170–1210°C) (Table 1 and Figure 10). A similar relationship has been observed with spreading rate along the global MOR system, i.e., that lavas from fast spreading ridges (high magma supply) have cooler eruption temperatures than lavas from slow-spreading ridges [*Sinton and Detrick*, 1992]. *Rubin and Sinton* [2007] emphasized the correlation between eruption temperature and magma chamber depth, and attributed this result to low but variable crustal temperatures at shallow depths where melt lenses reside at relatively fast spreading rates. Magma reservoirs are predicted to exist at greater depths at our low-magma-supply study area [*Blacic et al.*, 2004], where erupted lavas are generally hotter but less variable in eruption temperature, presumably because the mid- to lower

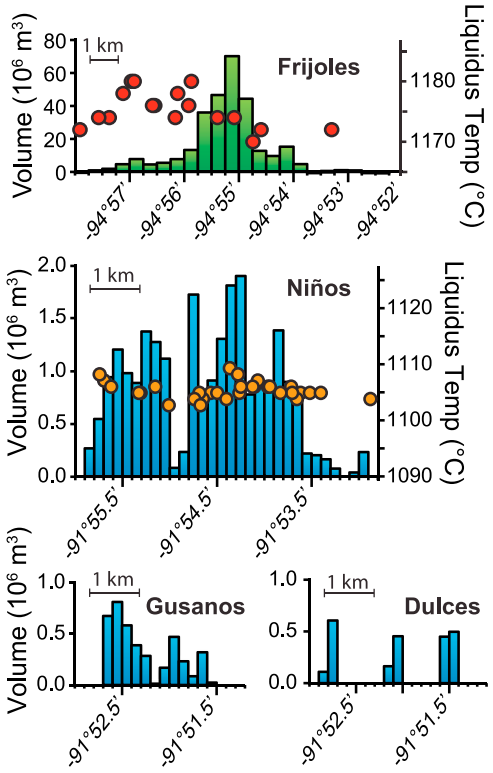

Figure 11. Along-axis variation in eruptive volume for fissure eruptions at low (Frijoles) and high (Niños, Gusanos, and Dulces) magma supply study areas. Eruptive units were binned by latitude (0.25 arc minute bins for Frijoles; 0.1 arc minute bins for other units) and volumes calculated as for unit volumes, using bathymetry and a horizontal basal surface. Red and orange dots in Frijoles and Niños plots show along-axis variations in liquidus temperatures (calculated using MELTS [*Ghiorso and Sack*, 1995; *Asimow and Ghiorso*, 1998]) for samples collected in each flow field. For both the Frijoles and Niños eruptions, the highest liquidus temperatures correspond to what are thought to be the earlier parts of the eruptions (see text for discussion).

crust is farther removed from the effects of vigorous hydrothermal cooling.

[48] Variations in MgO content (and calculated liquidus temperatures) are also documented within some of the most densely sampled individual eruptive units. Along the Frijoles eruptive fissure, the region with the greatest eruptive volume does not coincide with the highest temperatures (Figure 11). This result is similar to that for the N1 eruption along the SEPR, where *Bergmanis et al.* [2007, Figure 9] noted that the maximum erupted volume along axis corresponded with relatively low eruption temperatures and a local minimum in the AMC depth. In the case of the Frijoles eruption, it is unclear whether the variation in MgO records a spatial or temporal variation in lava temperatures and we lack data on the along-axis depths of the reservoir feeding the eruption. Cooler lava temperatures could be erupted from regions where the AMC is shallower, or conceivably from the cooler edges or ends of the melt reservoir, although the latter seems unlikely to coincide with high eruption volumes. Alternatively, it is possible that lava temperatures along the length of the eruptive fissure were initially high, and cooled progressively during the course of the eruption. In this case, one might find the lowest temperatures where effusion continued the longest (see section 7.4).

7.3. Eruptive Volume

[49] Eruptive volumes of low-relief units (smooth flows) and higher-relief units (hummocky mounds and ridges and seamounts) within our study areas were estimated using two different methods. For relatively high-relief units, we assume a pre-existing horizontal basal surface at the average depth of the unit's boundary, and calculate the volume between this surface and the mapped seafloor depth. The assumption of a horizontal basal surface results in an overestimate of unit volumes if the mapped unit buried pre-existing edifices, and an underestimate if the flow unit filled pre-existing depressions.

[50] For the low-relief Del Norte flow field, we multiplied the mapped lava flow area by an average thickness of 15 m (based on observed collapse depths, flow front heights, and the thicknesses of flows exposed on fault scarps) to obtain a flow unit volume, similar to methods of *Gregg et al.* [1996], *Sinton et al.* [2002], and *Soule et al.* [2007] for low-relief units along the EPR. The 15-m thickness that we estimate is significantly greater than the 1–2 m used by *Soule et al.* [2007] for the latest eruption at 9°50′ N along the EPR, but is similar to the maximum thickness of the 2011 Axial volcano flow field (as measured by repeat bathymetric surveys) where it "filled a shallow depression and inflated" [*Caress et al.*, 2012]. The Del Norte flow field occurs within a similar confining structure, provided by the axial graben, and appears to have had a similar emplacement history.

[51] The areas and estimated volumes of mapped flow fields are presented in Table 2. For Del Norte and Calor, each of which was partially buried by successive eruptions, we present an additional estimate of the total (original) area and eruptive volume. In several other cases (Cobija, Cocodrilo,

Table 2. GSC Lava Flows: Dimensions and Descriptions

Flow Field Name	Mapped Unit Length (km)	Mapped Outcrop Area (km^2)	Volume (km^3)	Comments
		Low Magma Supply		
Frijoles	10.8	6.2	0.28	youngest mapped unit at low magma supply study area: discontinuous chain of pillow mounds
Del Norte	6.0	8.2 (9.4)[a]	0.12 (0.14)[a]	predominantly sheet and lobate flows erupted from north of axial graben; locally, small pillow mounds
Buho	7.1	14.6	1.31	axial seamount with summit collapse craters flanked by smaller, clusters of highly ornamented pillow mounds
Tortuga	2.3	3.9	0.36	axial seamount; summit region predominantly inflated, partially collapsed flows
Dragón	2.0	1.8	0.09	irregular, steep-sided cluster of slightly ornamented pillow mounds, roughly centered within axial graben
Pulgar	1.8	2.0	0.12	cluster of unornamented pillow mounds; most mounds have summit plateaus where lobate flows predominate
Pinguino	2.1	3.0	0.24	axial seamount; summit region predominantly inflated, partially collapsed flows
Altares	3.7	3.5	0.10	irregularly shaped cluster of pillow mounds; 100-m tall pinnacle rises from summit plateau of largest mound
		High Magma Supply		
Niños	6.1	2.0	0.03	youngest mapped unit in high-magma-supply study area: pillow ridge with recent hydrothermal activity
Calor	8.3	3.5 (5.3)[a]	0.03 (0.05)[a]	intermediate-aged pillow ridge hosting several actively venting hydrothermal chimneys
Empanada	3.5	3.9	0.13	small axial seamount and associated low-lying sheet flows
Dulces	2.7	0.1	0.002	discontinuous chain of small pillow mounds
Gusanos	2.1	0.3	0.005	discontinuous pillow ridges aligned along spreading axis
Iguana	5.5	0.7	–[b]	pillows, lobate flows, and jumbled to hackly sheet flows, partially buried by more recent units
Cocodrilo	9.6	2.2	–	broad mounds made up mostly of pilllow and lobate flows, partially buried by more recent units
Lobo del Mar	1.7	0.6	–	chain of eruptive vents, channels, and associated off-axis lava lake (partially collapsed)
Lagarto	–	0.3	–	pillow, lobate, and channelized sheet flows.
Cobija	5.6	2.4	–	oldest mapped flow field: low-relief pillow, lobate, and sheet flows

[a]Areas and volumes in parentheses include regions presumed to have been buried by later eruptive activity (Del Norte; Calor).
[b]Dashes indicate units for which sufficient outcrop does not exist to make reasonable estimates of volume.

Iguana, Lagarto, Lobo del Mar), there has been too much post-eruptive faulting and/ or burial to make reasonable estimates of original flow field areas and hence, eruptive volumes. Additionally, we have not attempted to account for the possibility that some eruptions (particularly those located near the boundaries of each study area) extended along axis outside the study areas.

[52] Bearing in mind the uncertainties associated with the estimation of flow field thicknesses and original outcrop areas, our results indicate that erupted volumes range over one to two orders of magnitude at each study area, similar to the variation in eruptive volume documented at other locations along the MOR system [*Perfit and Chadwick*, 1998; *Sinton et al.*, 2002].

[53] Mapped eruptive volumes at the low-magma-supply study area are greater on average, and range to significantly greater values (0.091–1.3 km^3) than those at the high-magma-supply study area (0.0022–0.13 km^3). The inverse correlation between magma supply and average eruptive volume along the GSC agrees with that between spreading rate and eruptive volume proposed for the global MOR system [*Perfit and Chadwick*, 1998; *Sinton et al.*, 2002]. We show here, however, that significant variations in average eruptive volume can arise from variations in magma supply, independent of spreading rate (Figure 12).

[54] Axial seamounts with broad summit plateaus are consistently the largest eruptive units at both study areas; these features are larger and more

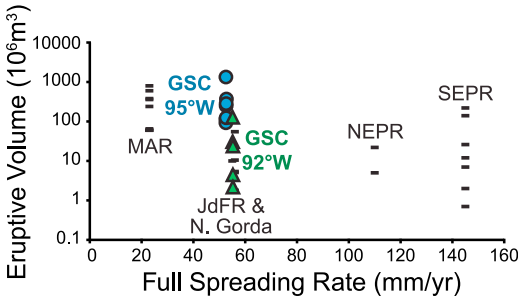

Figure 12. Eruptive volume variations versus spreading rate. Variability in eruptive volume for eruptions on most ridges is at least an order of magnitude (exception is northern East Pacific Rise, for which there are only two documented eruptions). GSC eruptive volumes demonstrate non-spreading rate-related variation in eruptive volume. GSC volumes are reported in this paper. Those from other ridges are from *Sinton et al.* [2002], *Soule et al.* [2007], and references therein. MAR, Mid-Atlantic Ridge; JdFR & N. Gorda, Juan de Fuca and North Gorda Ridges; NEPR, northern East Pacific Rise; SEPR, southern East Pacific Rise.

common at the low-magma-supply study area. Empanada is the only axial seamount within the high-magma-supply study area. *Smith and Cann* [1992] used a magmastatic model to argue that the height of eruptive edifices with large summit plateaus is limited by the depth of the magma reservoir feeding the eruption, with greater depths required to produce tall seamounts. Empanada's height (~100 m) agrees remarkably well with the prediction of the *Smith and Cann* model for an AMC depth of 1.7 km (the depth of the seismically imaged melt lens at high magma supply). If this model holds for the low-magma-supply study area, where we lack seismic imaging of an AMC, the magma reservoirs feeding the Buho, Pinguino, and Tortuga eruptions should have been 2.5–3 km deep.

[55] Both the Buho and Empanada seamounts represent highstanding parts of eruptive units that are surrounded by co-eruptive, lower relief smooth flows or hummocks. Although we do not have temporal resolution within these eruptive sequences, a likely scenario is that the eruptions began as longer fissures that progressively closed down to long-lived centers at the location of the seamounts [e.g., *Wadge*, 1981]. Thus at least some MOR axial seamounts represent only parts of more extensive eruptive sequences. Buho and Empanada are relatively young features and their flanks have not been completely obscured by later activity. Whether or not other axial seamounts, including older features like Pinguino or Tortuga, might also represent the highstanding remnants of more extensive lava sequences is unclear.

7.4. Eruption Recurrence Intervals

[56] There are three submarine locations where multiple eruptions have been observed (9°50′N EPR, Axial Seamount (JdFR), and the Coaxial segment of the JdFR) (see *Rubin et al.* [2012] for review). Eruption recurrence intervals are 10–20 years in each of these locations, although it is unclear how representative the associated eruption recurrence intervals are of eruptive activity over longer time periods [*Rubin et al.*, 2012]. In the absence of repeat eruptions, three general approaches have been used to calculate eruption recurrence intervals along other MOR's: calculating the number of meter-wide diking events needed to accommodate seafloor spreading [e.g., *Hooft et al.*, 1996; *Curewitz and Karson*, 1998]; dating sequences of lava flows, using one or a combination of radiometric techniques, geomagnetic paleointensity, and sediment thickness [*Bergmanis et al.*, 2007]; and using the average eruptive volume and time-averaged rate of production of extrusive lavas [*Perfit and Chadwick*, 1998; *Sinton et al.*, 2002].

[57] Simple estimates based on meter-wide dikes overestimate eruptive frequencies because not all intruded dikes reach the surface (25–50% in Hawai'i and Iceland [e.g., *Hooft et al.*, 1996]). Furthermore, there could be systematic variations in the fraction of dikes that erupt depending on, for example, the rate of magma supply, regional stress state, and depth of the reservoirs from which dikes initiate [*Behn et al.*, 2006; *Buck et al.*, 2006; *Bialas et al.*, 2010]. In addition, the percent of spreading accommodated by faulting (as opposed to diking) appears to vary systematically with spreading rate; estimates presented by *Cowie et al.* [1993] suggest that at the slow-spreading MAR, 10–20% of spreading is accommodated by faulting, compared with 5–10% along the fast spreading EPR. The spreading rates of 53 and 55 mm/yr at our study areas [*Argus et al.*, 2011] generate essentially indistinguishable diking recurrence intervals of 19 and 18 years for 1-m wide dikes at the low-and high-magma-supply study areas, respectively, assuming steady state diking behavior.

[58] Constraints from geomagnetic paleointensity measurements at the high-magma-supply study area suggest that there have been at least six eruptions along one 10 km-long ridge segment in the past 400 years [*Bowles et al.*, 2011], yielding an average

eruption recurrence interval of 67 years. The paleointensity data suggest that eruptions within this region might be episodic, with hundreds of years of relative quiescence in the interval between the 400 year-old eruption and several more recent eruptions that appear to cluster more closely in time [*Bowles et al.*, 2011]. A several-hundred-year period between eruptive episodes approaches the recurrence intervals of recent rifting phases along slow-spreading subaerial ridges in Iceland and Ethiopia [e.g., *Wright et al.*, 2012]. Qualitative observations of sediment thickness at the two GSC study areas suggest that the intervals between eruptions are longer at low magma supply, where there are greater differences in sediment cover between successive eruptive units.

[59] Using the spreading rate [*Argus et al.*, 2011], thickness of seismic layer 2A [*Blacic et al.*, 2004], and estimated eruptive volumes, we can generate a third estimate for the eruption recurrence interval required to build the extrusive layer at each study area. Layer 2A is thicker at the low-magma-supply area (0.6 km and 0.4 km at low- and high-magma-supply study areas, respectively) [*Blacic et al.*, 2004], so the volumetric rate of production of layer 2A is actually greater there. Because the median eruptive volume is also greater at low magma supply, the calculated median eruption recurrence interval is ~4 times longer near 95°W (183 years along a 25 km-long ridge segment versus 46 years at high magma supply).

7.5. Average Effusion Rates

[60] Analog modeling studies have shown that submarine lava morphology is controlled by the relative rates of heat loss and lateral advection of a flow, with efficiently cooled or slowly moving flows producing pillow lavas, inefficiently cooled or quickly moving flows producing sheet flows [e.g., *Griffiths and Fink*, 1992; *Gregg and Fink*, 1995], and lobate flows having intermediate characteristics. At a given location, the rate of cooling is unlikely to vary greatly, but there may be significant variation in the rate of advection caused by differences in effusion rate, slope, and lava viscosity. Flow morphology in submarine lava flow fields has been used as a proxy for eruption rate [e.g., *Gregg et al.*, 1996], but to derive actual rates, reasonable estimates of lava viscosity and preexisting slopes must be employed.

[61] Along the GSC, we can use observed lava morphologies to qualitatively compare effusion rates within eruptive units and more generally between the two study areas (Table 2). Pillow lavas are the most common lava morphology at both study areas, but lobate and sheet flows account for a larger proportion of flows at high magma supply. Using an automated seafloor classification system, *McClinton et al.* [2012] mapped lava morphology within the high-magma-supply study area, and found 47% pillows, 31% lobates, and 12% sheets. Similar work in the low-magma-supply study area found 85% pillows, 5% lobates, and 5% sheets (J. McClinton, personal communication, 2011). These estimates are consistent with observations during dives and camera tows, which indicated that sheet flows were rare in the low-magma-supply study area, with the exception of parts of the Del Norte flow field, and that lobate flows were generally restricted to the summits of hummocks and seamounts. Correlations between lava morphology and spreading rate (and, thus, magma supply) have been observed elsewhere [e.g., *Bonatti and Harrison*, 1988; *Perfit and Chadwick*, 1998; *Meyer and White*, 2007]. Similarly, studies of lava morphology within individual spreading center segments at 9°N and 16–19°S along the EPR indicate that low-effusion rate eruptions are more common at discontinuities in the ridge axis, where eruptive activity is distributed over a wider region across axis [*White et al.*, 2002, 2009].

[62] Our lava morphology observations suggest that effusion rates are, on average, greater at the high-magma-supply study area, despite evidence that eruptions with a range of effusion rates have occurred in both study areas. Analog models predict that decreasing viscosity will also cause lava morphology to transition from pillow to lobate to sheet flows, even at a constant effusion rate [e.g., *Gregg and Fink*, 1995]. Melt viscosity is affected by temperature, major element composition, and volatile content [e.g., *Giordano et al.*, 2008]. Although the lower silica and higher alkali and water contents of glasses from the high-magma-supply study area [*Cushman et al.*, 2004] would tend to lower lava viscosity there for a given temperature and MgO content, the higher degrees of fractionation and lower liquidus temperatures at the high-magma-supply study area have a counter-balancing effect. Viscosity calculations using the method of *Giordano et al.* [2008] yield liquidus melt viscosities ranging up to 340 Pa-s at high magma supply, compared to a maximum liquidus melt viscosity of 70 Pa-s at low magma supply (Figure 10).

[63] Using viscosity and lava morphology to estimate actual effusion rates for each eruption (or for different phases of individual eruptions) requires

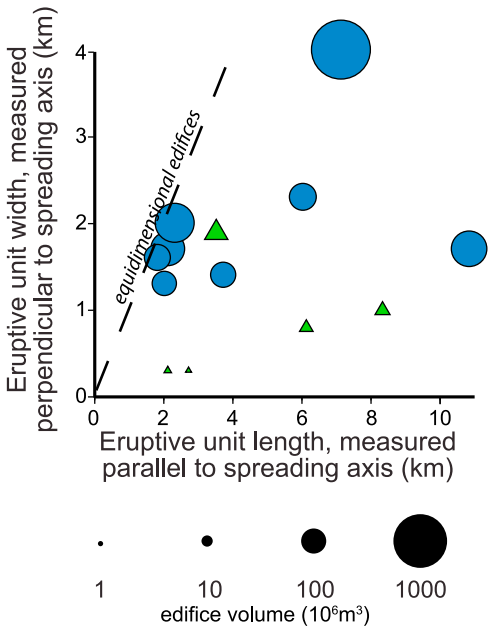

Figure 13. Plan view geometry of mapped eruptive units. Symbol size corresponds to flow field volume. Blue circles, low-magma-supply study area; green triangles, high-magma-supply study area.

consideration of crystallinity and crystal morphology, which can increase the bulk viscosity by orders of magnitude [e.g., *Costa et al.*, 2009; *Vona et al.*, 2011]. Quantification of these parameters is beyond the scope of the present discussion, but several examples demonstrate that to first order, the observed variations in lava morphology are not simply a function of bulk magma viscosity. The Buho eruption in the low-magma-supply study area has one of the lowest liquidus melt viscosities (averaging 22 Pa-s), and is essentially aphyric, but all mapped regions of the flow field contain ornamented pillow lavas indicative of low effusion rates, even on steep seamount flanks. In contrast, Del Norte has the same liquidus melt viscosity and slightly higher crystallinity, but flow morphologies range from pillows to sheets. These observations require variations in effusion rate that are independent of lava viscosity.

[64] Observations of eruptive edifice morphologies at each study area provide additional constraints on effusion rates. Laboratory experiments and models of magma flow within a dike indicate that high flow rates are required to maintain effusion along the length of a fissure [e.g., *Wadge*, 1981; *Bruce and Huppert*, 1989; *Whitehead and Helfrich*, 1991; *Head et al.*, 1996]. Magma flowing through a dike is cooled by conduction through the dike walls, causing increased viscosity and consequently decreased velocity. Conduit widths decrease where magma freezes along the dike walls; conversely, in regions of greater flow, thermal erosion of the dike walls is possible [*Wadge*, 1981]. If the effusion rate is not sufficient to maintain an open channel within the dike, flow will cease. The prevalence of moderately long fissure eruptions (Figure 13) at the high-magma-supply study area supports the interpretation that effusion rates are generally higher there than at the low-magma-supply study area, since high effusion rates should allow more of the fissure length to remain active for longer durations. It is notable, however, that the longest eruptive fissure recognized in either area is the Frijoles eruption in the low-magma-supply area. Prolonged effusion along a fissure could effectively decrease the elongation of the associated flow field (the ratio of the flow field's length to its width), as lavas are emplaced away from the fissure itself, but the length of the fissure along which lava is erupted should still reflect the effusion rate at the time the fissure was active, assuming the entire length of the fissure was active at once.

[65] Variations in lava morphology and eruptive edifice morphology within several of the mapped lava flow fields indicate spatial and temporal variations in effusion rate over the course of individual eruptive episodes. The Del Norte, Niños, and Empanada flow fields each include extensive low-lying regions where sheet flows predominate, overlain by localized pillow mounds; these sequences suggest an initial high effusion rate phase after which effusion rates waned [*McClinton et al.*, 2011]. Similarly, the along-axis distribution of lava along the Frijoles, Buho and Empanada flow fields indicates a focusing of flow near the center of what were probably the initial eruptive fissures (Figure 11). These eruptive histories are consistent with decreasing effusion rates and localization of flow observed during subaerial basaltic fissure eruptions in Iceland [*Wadge*, 1981; *Thorarinsson et al.*, 1973; *Harris et al.*, 2001] and Hawai'i [*Richter et al.*, 1973; *Lockwood et al.*, 1987], and inferred from seafloor observations on the MAR [*Ballard and van Andel*, 1977]. Other hummocky ridges, such as the Gusanos and Niños eruptive units at the high-magma-supply study area, appear to have less flow localization (Figure 11).

[66] Despite the evidence for variable eruption rates within some eruptions, the combined flow morphology and eruptive edifice morphology observations strongly suggest that average effusion rates are higher at the high-magma-supply site, and that the

observed variations cannot be attributed to differences in magma viscosity. The high effusion rates at high magma supply could be caused by higher average magma driving pressures in the high supply magma reservoirs. The declining eruption rates and flow localization of several units during the course of the eruptions may have been driven by declining magma driving pressures late in the eruptive episodes.

8. Relevance to Other Mid-ocean Ridges

[67] The increase in magma supply along the GSC is associated with proximity to the Galápagos hot spot, which affects magma chemistry and crustal structure in ways that would not be expected at MOR's unaffected by hot spots. Despite this abnormality, the increased magma supply near the hot spot allows a melt lens to persist at shallow depths within the crust, and the higher average degrees of fractionation observed along the GSC associated with this shallow melt lens is entirely consistent with global ridge systematics [e.g., *Rubin and Sinton*, 2007]. However, hot spot-related enrichments in H_2O and incompatible elements at a given MgO content in our high-magma-supply area [e.g., *Cushman et al.*, 2004; *Ingle et al.*, 2010] are not typical of most fast spreading ridges. The elevated H_2O content, in particular, should decrease melt viscosity, with potential increases in effusion rates and the abundance of sheet flows relative to pillow lavas. Nevertheless, an increase in fissure eruptions at our high-magma-supply study area is consistent with the observed trend with increasing magma supply normally associated with spreading rate [*Sinton et al.*, 2002], even though it may be augmented by differences in melt viscosity that are uncharacteristic of melt supply at "normal" ridges.

[68] Although the GSC provides a rare opportunity to isolate the effects of variable magma supply from those of spreading rate, these two parameters are coupled along most of the global MOR system. To facilitate comparison with other ridges, we calculate the equivalent "normal" MOR spreading rate for each study area as the product of crustal thickness and spreading rate, assuming a uniform, 6 km-thick crust. The equivalent spreading rates are 50 and 67 mm/yr for the low and high-magma-supply study areas, respectively, both within the range of intermediate spreading rates. Thus the difference in spreading rates (and rates of magma supply) considered here is only about 10% of the total range in spreading rates in the global MOR system. It is therefore perhaps surprising that our observations indicate profound differences in eruption characteristics over such a small difference in overall supply. But eruption characteristics correlate well with magma chamber depth along the GSC, illustrating the sensitivity of magma chamber depth to small variations in magma supply at intermediate spreading rates [e.g., *Small and Sandwell*, 1989; *Purdy et al.*, 1992; *Sinton and Detrick*, 1992].

9. Conclusions

[69] Detailed mapping of eruptive units at low- and high-magma-supply study areas along the GSC allows us to quantify the range in eruption characteristics within each study area. At both study areas, the frequent juxtaposition of different flow fields with compositions that cannot be related by simple fractional crystallization is consistent with melt reservoirs that are either discontinuous or poorly mixed along axis, or replenished with compositionally distinct magmas at time scales that approach the eruption recurrence interval. Systematic variations in average lava temperature, eruptive volume, lava morphology, and eruptive unit morphology with increasing magma supply are generally consistent with those observed globally with increasing spreading rate.

[70] Eruptions within our high-magma-supply study area commonly have magma ascent rates sufficient to sustain eruptions along fissures greater than 5 km in length (assuming entire fissure lengths are active simultaneously). Lava temperatures within the study area vary by over ~100°C, and moderate to high degrees of fractionation are typical. The vast majority of these eruptions appear to be fed by the seismically imaged, mid-crustal AMC, which is thought to be a persistent feature at the high-magma-supply study area. Preliminary constraints suggest that the average repose period between highly episodic major rifting and eruption episodes is on the order of several decades.

[71] At our lower-magma-supply study area, eruptions tend to be larger in volume and less frequent (with repose periods of hundreds of years), have lower average effusion rates, and are more likely to focus to a point source. Magma chambers at low magma supply are thought to reside deeper within the crust, although a melt lens has not been seismically imaged at the low-magma-supply study area, and erupted lava temperatures are correspondingly hotter and more uniform. Long-lived, slow eruptions of large volumes of crystal-bearing lava (less

than 15% phenocrysts) have built much of the upper oceanic crust in this region.

[72] Whereas the variation in typical eruptive activity between the two study areas provides insight into the dependence of MOR eruptive processes on magma supply and consequent depths of magma reservoirs, the variability in eruptive characteristics can be used to place constraints on the range of conditions that are possible at each study area. Uncommon high-effusion-rate fissure eruptions of low-viscosity lava occur in the low-magma-supply area, and point-source edifices can form in the high-magma-supply area. These observations indicate that a range of stress states and magma chamber conditions are possible at a given location. Several individual eruptive units exhibit a range of edifice and lava morphologies that suggest eruption rates declined during the course of ongoing eruptions.

[73] This study demonstrates the variability of eruptive processes within two areas characterized by quantified differences in long-term magma supply that are not associated with changes in spreading rate. It is only because we have multiple examples within each area that systematic differences between areas become evident. Although the differences in average characteristics between areas generally accord with our present understanding of the effect of variable magma supply on magma chamber depths and attendant magmatic processes, the variability within areas has not been previously documented. It is clear that similar systematic investigations over a wide range of other ridges will be required to better understand the fundamental processes controlling the variability of eruptive processes, within and between eruptions, and to constrain the effects of larger variations in magma supply on eruptive processes.

Acknowledgments

[74] We are grateful to the *Alvin*, *Sentry*, and *TowCam* teams and to the crew of *R/V Atlantis* Cruise AT15–63 for their assistance with data acquisition at sea. We especially acknowledge Captain A. D. Colburn and Expedition Leader Bruce Strickrott for their contributions to this cruise. We thank the Ecuadorian government and the Parque Nacional Galápagos for permission to work in their territorial waters, and the staff of the Charles Darwin Research Foundation for help with logistics. Dan Fornari helped immensely with pre- and post-cruise logistics and ensured the readiness of the TowCam system. Mike Perfit and David Ferguson provided thorough and helpful reviews that improved the manuscript, and Scott Rowland is thanked for comments on an earlier version. JoAnn Sinton, Mary Tardona, and Eric Hellebrand helped with sample preparation and microprobe analyses. This work was supported by the National Science Foundation grants OCE08–49813, OCE08–50052, and OCE08–49711. This is SOEST contribution 8718.

References

Argus, D. F., R. G. Gordon, and C. DeMets (2011), Geologically current motion of 56 plates relative to the no-net-rotation reference frame, *Geochem. Geophys. Geosyst.*, *12*, Q11001, doi:10.1029/2011GC003751.

Asimow, P. D., and M. S. Ghiorso (1998), Algorithmic modification extending MELTS to calculate subsolidus phase relations, *Am. Mineral.*, *83*, 1127–1131.

Auzende, J.-M., et al. (1996), Recent tectonic, magmatic, and hydrothermal activity on the East Pacific Rise between 17 and 19 S: Submersible observations, *J. Geophys. Res.*, *101*, 17,995–18,010.

Ballard, R. D., and T. H. van Andel (1977), Morphology and tectonics of the inner rift valley at lat 36°50′N on the Mid-Atlantic Ridge, *Geol. Soc. Am. Bull.*, *88*, 507–530.

Behn, M. D., J. M. Sinton, and R. S. Detrick (2004), Effect of the Galápagos hotspot on seafloor volcanism along the Galápagos Spreading Center (90.9–97.6°W), *Earth Planet. Sci. Lett.*, *217*, 331–347.

Behn, M. D., W. R. Buck, and I. S. Sacks (2006), Topographic controls on dike injection in volcanic rift zones, *Earth Planet. Sci. Lett.*, *246*, 188–196.

Bergmanis, E. C., J. Sinton, and K. H. Rubin (2007), Recent eruptive history and magma reservoir dynamics on the southern East Pacific Rise at 17°30′S, *Geochem. Geophys. Geosyst.*, *8*, Q12O06, doi:10.1029/2007GC001742.

Bialas, R. W., W. R. Buck, and R. Qin (2010), How much magma is required to rift a continent?, *Earth Planet. Sci. Lett.*, *292*, 68–78.

Blacic, T. M., G. Ito, J. P. Canales, R. S. Detrick, and J. Sinton (2004), Constructing the crust along the Galapaogs Spreading Center 91.3°–95.5°W: Correlation of seismic layer 2A with axial magma lens and topographic characteristics, *J. Geophys. Res.*, *109*, B10310, doi:10.1029/2004JB003066.

Bonatti, E., and C. G. A. Harrison (1988), Eruption style of basalt in oceanic spreading ridges and seamounts: Effect of magma temperature and viscosity, *J. Geophys. Res.*, *93*, 2967–2980.

Bonatti, E., M. Ligi, D. Brunelli, A. Cipriani, P. Fabretti, V. Ferrante, L. Gasperini, and L. Ottolini (2003), Mantle thermal pulses below the Mid-Atlantic Ridge and temporal variations in the formation of oceanic lithosphere, *Nature*, *423*, 499–505.

Bowles, J., J. S. Gee, D. V. Kent, M. R. Perfit, S. A. Soule, and D. J. Fornari (2006), Paleointensity applications to timing and extent of eruptive activity, 9°–10°N East Pacific Rise, *Geochem. Geophys. Geosyst.*, *7*, Q06006, doi:10.1029/2005GC001141.

Bowles, J. A., A. Ab Fatah, A. Colman, J. T. McClinton, J. M. Sinton, S. M. White, and K. H. Rubin (2011), Geomagnetic paleointensity constraints on eruption timing at the Galápagos Spreading Center, Abstract V53D-2657 presented at 2011 Fall Meeting, AGU, San Francisco, Calif., 5–9 Dec.

Bruce, P. M., and H. E. Huppert (1989), Thermal control of basaltic fissure eruptions, *Nature*, *342*, 665–667.

Buck, W. R., P. Einarsson, and B. Brandsdottir (2006), Tectonic stress and magma chamber size as controls on dike propagation: Constraints from the 1975–1984 Krafla rifting episode, *J. Geophys. Res.*, *111*, B12404, doi:10.1029/2005JB003879.

Byerly, G. R., W. G. Melson, and P. R. Vogt (1976), Rhyodacites, andesites, ferrobasalts and ocean tholeiites from the Galápagos Spreading Center, *Earth Planet. Sci. Lett.*, *30*, 215–221.

Canales, J. P., R. S. Detrick, J. Lin, J. A. Collins, and D. R. Toomey (2000), Crustal and upper mantle seismic structure beneath the rift mountains and across a nontransform offset at the Mid-Atlantic Ridge (35°N), *J. Geophys. Res.*, *105*(B2), 2699–2719.

Canales, J. P., G. Ito, R. S. Detrick, and J. Sinton (2002), Crustal thickness along the western Galápagos Spreading Center and the compensation of the Galápagos hotspot swell, *Earth Planet. Sci. Lett.*, *203*, 311–327.

Caress, D. W., D. A. Clague, J. B. Paduan, J. F. Martin, B. M. Dreyer, W. W. Chadwick, A. Denny, and D. S. Kelley (2012), Repeat bathymetric surveys at 1-metre resolution of lava flows erupted at Axial Seamount in April 2011, *Nat. Geosci.*, *5*, 483–488, doi:10.1038/ngeo1496.

Chadwick, W. W., and R. W. Embley (1994), Lava flows from a mid-1980s submarine eruption on the Cleft segment, Juan de Fuca Ridge, *J. Geophys. Res.*, *99*, 4761–4776.

Chadwick, W. W., R. W. Embley, and C. G. Fox (1995), SeaBeam depth changes associated with recent lava flows, CoAxial segment, Juan de Fuca Ridge: Evidence for multiple eruptions between 1981–1993, *Geophys. Res. Lett.*, *22*, 167–170.

Chadwick, W. W., R. W. Embley, and T. M. Shank (1998), The 1996 Gorda Ridge eruption: Geologic mapping, sidescan sonar, and SeaBeam comparison results, *Deep Sea Res., Part II*, *45*, 2547–2569.

Costa, A., L. Caricchi, and N. Bagdassarov (2009), A model for the rheology of particle-bearing suspensions and partially molten rocks, *Geochem. Geophys. Geosyst.*, *10*, Q03010, doi:10.1029/2008GC002138.

Cowie, P. A., C. H. Scholz, M. Edwards, and A. Malinverno (1993), Fault strain and seismic coupling on mid-ocean ridges, *J. Geophys. Res.*, *98*(B10), 17,911–17,920.

Crisp, J. A. (1984), Rates of magma emplacement and volcanic output, *J. Volcanol. Geotherm. Res.*, *20*, 177–211.

Curewitz, D., and J. A. Karson (1998), Geological consequences of dike intrusion at mid-ocean ridge spreading centers, in *Faulting and Magmatism at Mid-ocean Ridges*, *Geophys. Monogr. Ser.*, vol. 106, edited by W. R. Buck, pp. 117–136, AGU, Washington, D. C.

Cushman, B., J. Sinton, G. Ito, and J. E. Dixon (2004), Glass compositions, plume-ridge interaction, and hydrous melting along the Galápagos Spreading Center, 90.5°W to 98°W, *Geochem. Geophys. Geosyst.*, *5*, Q08E17, doi:10.1029/2004GC000709.

Dziak, R. P., and C. G. Fox (1999), The January 1998 earthquake swarm at Axial Volcano, Juan de Fuca Ridge, Hydroacoustic evidence for seafloor volcanic activity, *Geophys. Res. Lett.*, *26*, 3425–3428.

Eason, D. E., and J. M. Sinton (2009), Lava shields and fissure eruptions of the Western Volcanic Zone, Iceland: Evidence for magma chambers and crustal interaction, *J. Volcanol. Geotherm. Res.*, *186*, 331–348, doi:10.1016/j.jvolgeores.2009.06.009.

Ebinger, C., A. Ayele, D. Keir, J. Rowland, G. Yirgu, T. Wright, M. Belachew, and I. Hamling (2010), Length and timescales of rift faulting and magma intrusion: The Afar rifting cycle from 2005 to present, *Annu. Rev. Earth Planet. Sci.*, *38*, 437–464, doi:10.1146/annurev-earth-040809-152333.

Embley, R. W., W. Chadwick, M. R. Perfit, and E. T. Baker (1991), Geology of the northern Cleft segment, Juan de Fuca Ridge: Recent lava flows, sea-floor spreading, and the formation of megaplumes, *Geology*, *19*, 771–775.

Embley, R. W., W. W. Chadwick, D. Clague, and D. Stakes (1999), The 1998 eruption of Axial Volcano: Multibeam anomalies and seafloor observations, *Geophys. Res. Lett.*, *26*, 3425–3428.

Embley, R. W., W. W. Chadwick, M. R. Perfit, M. C. Smith, and J. R. Delaney (2000), Recent eruptions on the CoAxial segment of the Juan de Fuca Ridge: Implications for mid-ocean ridge accretion processes, *J. Geophys. Res.*, *105*, 16,501–16,525.

Ferguson, D. J., T. D. Barnie, D. M. Pyle, C. Oppenheimer, G. Yirgu, E. Lewi, T. Kidane, S. Carn, and I. Hamling (2010), Recent rift-related volcanism in Afar, Ethiopia, *Earth Planet. Sci. Lett.*, *292*, 409–418, doi:10.1016/j.epsl.2010.02.010.

Fornari, D. J. (2003), A new deep-sea towed digital camera and multi-rock coring system, *Eos Trans. AGU*, *84*, 69–76, doi:10.1029/2003EO080001.

Fornari, D. et al. (2004), Submarine lava flow emplacement at the East Pacific Rise 9°50′N: Implications for uppermost ocean crust stratigraphy and hydrothermal fluid circulation, in *Mid-Ocean Ridges: Hydrothermal Interactions Between the Lithosphere and the Oceans*, *Geophys. Monogr. Ser.*, vol. 148, edited by C. R. German et al., pp. 187–217, AGU, Washington.

Fox, C. G. (1999), In situ ground deformation measurements from the summit of Axial Volcano during the 1998 volcanic episode, *Geophys. Res. Lett.*, *26*, 3437–3440.

Fox, C. G., K. M. Murphy, and R. W. Embley (1988), Automated display and statistical analysis of interpreted deep-sea bottom photographs, *Mar. Geol.*, *78*, 199–216.

Fox, C. G., W. E. Radford, R. P. Dziak, T.-K. Lau, H. Matsumoto, and A. E. Schreiner (1995), Acoustic detection of a seafloor spreading episode on the Juan de Fuca Ridge using military hydrophone arrays, *Geophys. Res. Lett.*, *22*, 131–134.

Fundis, A., S. Soule, D. J. Fornari, and M. R. Perfit (2010), Paving the seafloor: Volcanic emplacement processes during the 2005–2006 eruption at the fast-spreading East Pacific Rise, 9°50′N, *Geochem. Geophys. Geosyst.*, *11*, Q08024, doi:10.1029/2010GC003058.

Ghiorso, M. S., and R. O. Sack (1995), Chemical mass transfer in magmatic processes. IV. A revised and internally consistent thermodynamic model for the interpolation and extrapolation of liquid–solid equilibria in magmatic systems at elevated temperatures and pressures, *Contrib. Mineral. Petrol.*, *199*, 197–212.

Giordano, D., J. K. Russell, and D. B. Dingwell (2008), Viscosity of magmatic liquids: A model, *Earth Planet. Sci. Lett.*, *271*, 123–134, doi:10.1016/j.epsl.2008.03.038.

Goss, A. R., M. R. Perfit, W. I. Ridley, K. H. Rubin, G. D. Kamenov, S. A. Soule, A. Fundis, and D. J. Fornari (2010), Geochemistry of lavas from the 2005–2006 eruption at the East Pacific Rise, 9°46′N–9°56′N: Implications for ridge crest plumbing and decadal changes in magma chamber compositions, *Geochem. Geophys. Geosyst.*, *11*, Q05T09, doi:10.1029/2009GC002977.

Gregg, T. K. P., and J. H. Fink (1995), Quantification of submarine lava-flow morphology through analog experiments, *Geology*, *23*, 73–76.

Gregg, T. K. P., D. J. Fornari, M. R. Perfit, R. M. Haymon, and J. H. Fink (1996), Rapid emplacement of a mid-ocean ridge

lava flow on the East Pacific Rise at 9°46′–51′N, *Earth Planet. Sci. Lett.*, *144*, E1–E7.

Griffiths, R. W., and J. A. Fink (1992), Solidification and morphology of submarine lavas; a dependence on extrusion rate, *J. Geophys. Res.*, *97*, 19,729–19,737.

Grönvold, K., S. A. Halldorsson, G. Sigurdsson, G. Sverrisdottir, and N. Oskarsson (2008), The Krafla magma system—Isotopic constraints, paper presented at IAVCEI General Assembly, Int. Assoc. of Volcanol. and Chem. of the Earth's Inter, Reykjavík, Iceland.

Harris, A. J. L., J. B. Murray, S. E. Aries, M. A. Davies, L. P. Flynn, M. J. Wooster, R. Wright, and D. A. Rothery (2001), Effusion rate trends at Etna and Krafla and their implications for eruptive mechanisms, *J. Volcanol. Geotherm. Res.*, *102*, 237–270.

Haymon, R. M., et al. (1993), Volcanic eruption of the mid-ocean ridge along the East Pacific Rise crest at 9°45–52′N: Direct submersible observations of sea-floor phenomena associated with an eruption event in April, 1991, *Earth Planet. Sci. Lett.*, *119*, 85–101.

Head, J. W., L. Wilson, and D. Smith (1996), Mid-ocean ridge eruptive vent morphology and substructure: Evidence for dike widths, eruption rates, and evolution of eruptions and axial volcanic ridges, *J. Geophys. Res.*, *101*, 28,265–28,280.

Hey, R. N., M. C. Kleinrock, S. P. Miller, T. M. Atwater, and R. C. Searle (1986), SeaBeam/ Deep-Tow investigation of an active oceanic propagating rift system, Galápagos 95.5°W, *J. Geophys. Res.*, *91*(B3), 3369–3393.

Hooft, E. E., H. Schouten, and R. S. Detrick (1996), Constraining crustal emplacement processes from the variation in seismic layer 2A thickness at the East Pacific Rise, *Earth Planet. Sci. Lett.*, *142*, 289–309.

Ingle, S., G. Ito, J. J. Mahoney, W. Chazey, J. Sinton, M. Rotella, and D. M. Christie (2010), Mechanisms of geochemical and geophysical variations along the western Galápagos Spreading Center, *Geochem. Geophys. Geosyst.*, *11*, Q04003, doi:10.1029/2009GC002694.

Ito, G., and M. D. Behn (2008), Magmatic and tectonic extension at mid-ocean ridges: 2. Origin of axial morphology, *Geochem. Geophys. Geosyst.*, *9*, Q09O12, doi:10.1029/2008GC001970.

Kappel, E. S., and W. B. F. Ryan (1986), Volcanic episodicity and a non-steady state rift valley along northeast Pacific spreading centers: Evidence from Sea MARC I, *J. Geophys. Res.*, *91*, 13,925–13,940.

Kleinrock, M. C., and R. N. Hey (1989), Detailed tectonics near the tip of the Galápagos 95.5°W propagator: How the lithosphere tears and a spreading axis develops, *J. Geophys. Res.*, *94*, 13,801–13,838.

LeBas, M. J., and A. L. Streckeisen (1991), The IUGS systematics of igneous rocks, *J. Geol. Soc.*, *148*, 825–833.

Lockwood, J. P., J. J. Dvorak, T. T. English, R. Y. Koyanagi, A. T. Okamura, M. L. Summers, and W. R. Tanigawa (1987), Mauna Loa 1974–1984: A decade of intrusive and extrusive activity, *U.S. Geol. Surv. Prof. Pap.*, *1350*, 537–570.

Maclennan, J. (2008), Concurrent mixing and cooling of melts under Iceland, *J. Petrol.*, *49*, 1931–1953, doi:10.1093/petrology/egn052.

McClinton, J. T., S. M. White, J. M. Sinton, and A. Colman (2011), Effects of magma supply on seafloor construction: Insights from contrasting volcanic features along the Galápagos Spreading Center, 95W and 92W, Abstract V53D-2650 presented at 2011 Fall Meeting, AGU, San Francisco, Calif., 5–9 Dec.

McClinton, J. T., S. M. White, and J. M. Sinton (2012), Neuro-fuzzy classification of submarine lava flow morphology, *Photogramm. Eng. Remote Sens.*, *78*, 605–616.

Meyer, J. D., and S. M. White (2007), Lava morphology mapping by expert system classification of high-resolution side-scan sonar imagery from the East Pacific Rise, 9°–10°N, *Mar. Geophys. Res.*, *28*, 81–93.

Mitchell, N. C. (1998), Sediment accumulation rates from Deep Tow profiler records and DSDP Leg 70 cores over the Galápagos spreading center, in *Geological Evolution of Ocean Basins: Results From the Ocean Drilling Program*, edited by A. Cramp et al., *Geol. Soc. Spec. Publ.*, *131*, 199–209.

Mix, A. C., N. G. Pisias, R. Zahn, W. Rugh, C. Lopez, and K. Nelson (1991), Carbon 13 in Pacific deep and intermediate waters, 0–370 Ka: Implications for ocean circulation and Pleistocene CO_2, *Paleoceanography*, *6*, 205–226.

Perfit, M. R., and W. W. Chadwick (1998), Magmatism at mid-ocean ridges: Constraints from volcanological and geochemical investigations, in *Faulting and Magmatism at Mid-ocean Ridges*, *Geophys. Monogr. Ser.*, vol. 106, edited by W. R. Buck, pp. 59–116, AGU, Washington, D. C.

Purdy, G. M., L. S. L. Kong, G. L. Christeson, and S. C. Solomon (1992), Relationship between spreading rate and the seismic structure of mid-ocean ridges, *Nature*, *355*, 815–817.

Richter, D. H., J. P. Eaton, K. J. Murata, W. A. Ault, and H. L. Krivoy (1973), Chronological narrative of the 1959–1960 eruption of Kilauea volcano, Hawaii, *U.S. Geol. Surv. Prof. Pap.*, *537-E*, 1–73.

Rubin, K. H., and J. M. Sinton (2007), Inferences on mid-ocean ridge thermal and magmatic structure from MORB compositions, *Earth Planet. Sci. Lett.*, *260*, 257–276.

Rubin, K. H., J. D. Macdougall, and M. R. Perfit (1994), ^{210}Po-^{210}Pb dating of recent volcanic eruptions on the sea floor, *Nature*, *368*, 841–844.

Rubin, K. H., M. C. Smith, M. R. Perfit, D. M. Christie, and L. F. Sacks (1998), Geochronology and geochemistry of lavas from the 1996 North Gorda Ridge eruption, *Deep Sea Res., Part II*, *45*, 2571–2597.

Rubin, K. H., M. C. Smith, E. C. Bergmanis, M. R. Perfit, J. M. Sinton, and R. Batiza (2001), Geochemical heterogeneity within mid-ocean ridge lava flows: Insights into eruption, emplacement and global variations in magma generation, *Earth Planet. Sci. Lett.*, *188*, 349–367.

Rubin, K. H., M. R. Perfit, D. J. Fornari, S. A. Soule, M. Tolstoy, and F. Waldhauser (2006), Geochronology and composition of the 2005–06 volcanic eruptions of the East Pacific Rise, 9°46′–56′N, *Eos Trans. AGU*, *87*(52), Fall Meet. Suppl., Abstract V23B-0602.

Rubin, K. H., M. Tolstoy, D. J. Fornari, R. P. Dziak, S. A. Soule, F. Waldhauser, and K. L. von Damm (2008), Integrating radiometric, geophysical and thermal signals of volcanic unrest and eruption in 2005-06 at 97°50′N EPR, *Eos Trans. AGU*, *89*(53), Fall Meet. Suppl., Abstract B23F-07.

Rubin, K. H., S. A. Soule, W. W. Chadwick, D. J. Fornari, D. A. Clague, R. W. Embley, E. T. Baker, M. R. Perfit, D. W. Caress, and R. P. Dziak (2012), Volcanic eruptions in the deep sea, *Oceanography*, *25*, 142–157, doi:10.5670/oceanog.2012.12.

Ryan, W. B. F., et al. (2009), Global Multi-Resolution Topography synthesis, *Geochem. Geophys. Geosyst.*, *10*, Q03014, doi:10.1029/2008GC002332.

Saemundsson, K. (1991), Jardfraedi Kröflukerfisins, in *The Nature of Lake Myvatn* [in Icelandic], edited by A. Gardarson

and Á. Einarsson, pp. 2–95, Icelandic Nat. Sci. Soc., Reykjavík.

Sinton, J. M., and R. S. Detrick (1992), Mid-ocean ridge magma chambers, *J. Geophys. Res.*, *97*, 197–216.

Sinton, J. M., E. Bergmanis, K. Rubin, R. Batiza, T. K. P. Gregg, K. Grönvold, K. C. Macdonald, and S. M. White (2002), Volcanic eruptions on mid-ocean ridges: New evidence from the superfast spreading East Pacific Rise, 17°–19°S, *J. Geophys. Res.*, *107*(B6), 2115, doi:10.1029/2000JB000090.

Sinton, J., R. Detrick, J. P. Canales, G. Ito, and M. Behn (2003), Morphology and segmentation of the western Galápagos Spreading Center, 90.5°–98°W: Plume-ridge interaction at an intermediate spreading ridge, *Geochem. Geophys. Geosyst.*, *4*(12), 8515, doi:10.1029/2003GC000609.

Sinton, J., K. Grönvold, and K. Sæmundsson (2005), Postglacial eruptive history of the Western Volcanic Zone, Iceland, *Geochem. Geophys. Geosyst.*, *6*, Q12009, doi:10.1029/2005GC001021.

Small, C., and D. T. Sandwell (1989), An abrupt change in ridge axis gravity with spreading rate, *J. Geophys. Res.*, *94*(B12), 17,383–17,392.

Smith, D. K., and J. R. Cann (1992), The role of seamount volcanism in crustal construction at the Mid-Atlantic Ridge (24–30N), *J. Geophys. Res.*, *97*, 1645–1658.

Soule, S. A., D. J. Fornari, M. R. Perfit, and K. H. Rubin (2007), New insights into mid-ocean ridge volcanic processes from the 2005–06 eruption of the East Pacific Rise, 9°46′–56′N, *Geology*, *35*, 1079–1082, doi:10.1130/G23924A.1.

Stakes, D. S., M. R. Perfit, M. A. Tivey, D. W. Caress, T. Ramirez, and N. Maher (2006), The Cleft revealed: Geologic, magnetic, and morphologic evidence for construction of upper oceanic crust along the southern Juan de Fuca Ridge, *Geochem. Geophys. Geosyst.*, *7*, Q04003, doi:10.1029/2005GC001038.

Thorarinsson, S., S. Steinthórsson, T. Einarsson, H. Kristmannsdóttir, and N. Oskarsson (1973), The eruption on Heimaey, Iceland, *Nature*, *241*, 372–375.

Tolstoy, M., et al. (2006), A sea-floor spreading event captured by seismometers, *Science*, *314*, 1920–1922, doi:10.1126/science.1133950.

van Andel, T. H., and R. Ballard (1979), The Galápagos Rift at 86°W: 2. volcanism, structure, and evolution of the rift valley, *J. Geophys. Res.*, *84*, 5390–5406.

Vona, A., C. Romano, D. B. Dingwell, and D. Giordano (2011), The rheology of crystal-bearing basaltic magmas from Stromboli and Etna, *Geochim. Cosmochim. Acta*, *75*, 3214–3236, doi:10.1016/j.gca.2011.03.031.

Wadge, G. (1981), The variation of magma discharge during basaltic eruptions, *J. Volcanol. Geotherm. Res.*, *11*, 139–168.

White, S. M., K. C. Macdonald, and J. M. Sinton (2002), Volcanic mound fields on the East Pacific Rise, 16°–19°S: Low effusion rate eruptions at overlapping spreading centers for the past 1 Myr, *J. Geophys. Res.*, *107*(B10), 2240, doi:10.1029/2001JB000483.

White, S. M., J. D. Meyer, R. M. Haymon, and K. C. Macdonald (2008), High-resolution surveys along the hot spot-affected Galápagos Spreading Center: 2. Influence of magma supply on volcanic morphology, *Geochem. Geophys. Geosyst.*, *9*, Q09004, doi:10.1029/2008GC002036.

White, S. M., J. L. Mason, K. C. Macdonald, M. R. Perfit, V. D. Wanless, and E. M. Klein (2009), Significance of widespread low effusion rate eruptions over the past two million years for delivery of magma to the overlapping spreading centers at 9°N East Pacific Rise, *Earth Planet. Sci. Lett.*, *280*, 175–184.

Whitehead, J. A., and K. R. Helfrich (1991), Instability of flow with temperature-dependent viscosity: A model of magma dynamics, *J. Geophys. Res.*, *96*, 4145–4155.

Wilson, D. S., and R. N. Hey (1995), History of rift propagation and magnetization intensity for the Cocos-Nazca spreading center, *J. Geophys. Res.*, *100*, 10,041–10,056.

Wright, T. J., et al. (2012), Geophysical constraints on the dynamics of spreading centres from rifting episodes on land, *Nat. Geosci.*, *5*, 243–250, doi:10.1038/NGEO1428.